

Cell wall synthesis and remodeling dynamics determine bacterial division site architecture and cell shape

Authors

Paula P. Navarro^{1,2,†}, Andrea Vettiger^{3,†}, Virly Y. Ananda¹, Paula Montero Llopis⁴, Christoph Allolio⁵, Thomas G. Bernhardt^{*,3,6}, and Luke H. Chao^{*,1,2}

Affiliations

¹ Department of Molecular Biology, Massachusetts General Hospital, Boston, USA

² Department of Genetics, Blavatnik Institute, Harvard Medical School, Boston, USA

³ Department of Microbiology, Blavatnik Institute, Harvard Medical School, Boston, USA

⁴ MicRoN Core, Harvard Medical School, Boston, USA

⁵ Faculty of Mathematics and Physics, Mathematical Institute, Charles University, Prague, Czech Republic

⁶ Howard Hughes Medical Institute, Harvard Medical School, Boston

† These authors contributed equally, and sequence was determined alphabetically.

* To whom correspondence should be addressed (order determined alphabetically)

Thomas G. Bernhardt

Department of Microbiology, Harvard Medical School, Boston, USA

e-mail: thomas_bernhardt@hms.harvard.edu

Luke H. Chao

Department of Molecular Biology, Massachusetts General Hospital, Boston, USA

Department of Genetics, Harvard Medical School, Boston, USA

e-mail: chao@molbio.mgh.harvard.edu

Keywords

Bacterial cell division, Cell wall processing, Polar morphology, Cryo-electron tomography, Cryo-Focus Ion Beam milling, Fluorescence live-cell microscopy, Structured illumination microscopy

Abstract

The bacterial division apparatus builds daughter cell poles by catalyzing the synthesis and remodeling of the septal peptidoglycan (sPG) cell wall. Understanding of this essential process has been limited by the lack of native three-dimensional visualization of developing septa. Here, we used state-of-the-art cryogenic electron tomography (cryo-ET) and fluorescence microscopy to understand the division site architecture and sPG biogenesis dynamics of the Gram-negative bacterium *Escherichia coli*. Our results with mutant cells altered in the regulation of sPG biogenesis revealed a striking and unexpected similarity between the architecture of *E. coli* septa with those from Gram-positive bacteria, suggesting a conserved morphogenic mechanism. Furthermore, we found that the cell elongation and division machineries are in competition and that their relative activities determine the shape of cell constrictions and the poles they form. Overall, our results highlight how the activity of the division system can be modulated to generate the diverse array of morphologies observed in the bacterial domain.

Highlights

- The division site architecture of *E. coli* can be modulated to resemble that of diverse bacteria.
- Cell wall degradation at the division site activates septal cell wall synthesis.
- Assembly of the cytoskeletal ring at the division site is modulated by cell wall remodeling.
- Balance between the activities of the elongation and division systems modulates cell shape.

1 Introduction

2

3 Bacterial cells are typically surrounded by a multi-layered cell envelope that varies in complexity depending
4 on the species¹. Organisms classified as Gram-positive (monoderm) possess a single membrane
5 surrounded by a thick cell wall. Bacteria belonging to the Gram-negative (diderm) class have a thinner wall
6 layer to which a second membrane called the outer membrane (OM) is attached. Their cell wall is therefore
7 contained in an aqueous compartment called the periplasm that is sandwiched by the inner (cytoplasmic)
8 membrane (IM) and the OM². Understanding the mechanisms required for the biogenesis of bacterial
9 envelopes during cell growth and division has been a long-standing and fundamental goal of microbiology.
10 The process is also the target of many of our most widely used antibiotics. As such, studies of cell surface
11 assembly are of great practical significance due to the enabling insights they provide for the development
12 of new antibacterial treatments needed to combat the growing problem of drug-resistant infections.

13

14 The cell wall is the layer of the envelope that determines cell shape³. It is also critical for fortifying the
15 cytoplasmic membrane against osmotic lysis. The wall is assembled from the heteropolymer peptidoglycan
16 (PG), which consists of glycan chains with repeating disaccharide units of N-acetylglucosamine (GlcNAc)
17 and N-acetylmuramic acid (MurNAc). Short peptides are attached to each MurNAc sugar and are used to
18 form amide crosslinks between adjacent glycans, generating a covalently closed mesh around the
19 cytoplasmic membrane. Because the PG layer completely envelops the cell, its expansion and remodeling
20 are tightly coordinated with the cell cycle³.

21

22 Newborn rod-shaped cells like *Escherichia coli* first lengthen their cell body through the action of the
23 elongation machinery (Rod complex, elongasome), which synthesizes and incorporates new PG material
24 at dispersed locations throughout the cylinder³. Cell division is then initiated by the coalescence of
25 treadmilling polymers of the tubulin-like FtsZ protein into a structure called the Z-ring at midcell^{4,5}. The Z-
26 ring is peripherally associated with the IM and its formation ultimately results in the recruitment of dozens
27 of proteins to the prospective division site to assemble the envelope-spanning division machinery called
28 the divisome^{5,6}. A major function of this apparatus is to promote the localized synthesis of PG to generate
29 the cross-wall/septum that divides the daughter cell compartments³. The septal PG (sPG) produced by the
30 divisome initially connects the daughters such that it must be carefully processed to separate the newly
31 formed cells and complete the division process³.

32

33 Our understanding of envelope biogenesis during cell division has been greatly influenced by electron
34 micrographs of developing septa⁷. One of the most striking observations from these images is the extent
35 to which the septal architectures differ between organisms⁸. Some of the best images of septa from a
36 Gram-positive bacterium come from cryogenic electron microscopy of frozen vitrified sections (CEMOVIS)

37 of *Staphylococcus aureus*^{9,10}. In the septa of these cells, two tracks of PG material appear to be connected
38 to the lateral cell wall, forming an electron dense π structure with the two tracks located between the
39 invaginating membrane. Other Gram-positive bacteria like *Bacillus subtilis* are only observed to produce a
40 single, thick layer of cell wall within their septa^{11–14}. In contrast to the flat unconstricted side wall present at
41 Gram-positive division sites, conventional electron microscopy (EM) of fixed and stained cells and whole-
42 cell cryo-electron tomography (cryo-ET) imaging of *E. coli* and *Caulobacter crescentus* cells have
43 visualized a V-shaped constriction in which all three envelope layers are invaginating together^{15–17}.
44 Although the general presence of sPG can be observed in some images, the existence of sample
45 preparation artifacts and the low signal-to-noise ratio in conventional EM and cryo-ET images, respectively,
46 have prevented a clear visualization of its structural arrangement. However, notable morphological
47 differences between the division sites of *E. coli* and *C. crescentus* were evident in these images. Division
48 sites from *C. crescentus* displayed very tight coordination between the invagination of the three envelope
49 layers in all cells that were imaged¹⁶. They were never observed to form what would be considered a
50 classical crosswall septum in which a band of sPG bisects the cytoplasm. By contrast, some images of *E.*
51 *coli* showed a coordinately constricted envelope whereas others showed a partial crosswall where the IM
52 and PG layers seem more invaginated than the OM¹⁵. Whether these different septal architectures reflect
53 sample preparation artifacts, fundamental differences in the division mechanism between bacteria or arise
54 from changes in the spatiotemporal regulation of conserved processes remains a major outstanding
55 question.

56
57 To investigate the underlying mechanisms responsible for generating different division site morphologies,
58 we imaged the *in situ* ultrastructure of the division site and the dynamics of cell envelope constriction in
59 wild-type *E. coli* and several mutant derivatives with altered divisome function using cryo-ET and
60 fluorescence microscopy. For the cryo-ET analysis, we needed to overcome the major sample thickness
61 limitation of this imaging method in which samples > 300 nm in depth preclude the generation of
62 distinguishable contrast features by EM^{18,19}. This thickness limit is incompatible with the width of *E. coli*
63 and most other well-studied bacterial species that have cell diameters near 1 μm ²⁰. The development of
64 cryo-focused ion beam (cryo-FIB) milling^{21–27} made this imaging possible by allowing us to generate thin,
65 artifact-free lamellae of frozen-hydrated *E. coli* cells in various stages of division that are within the optimal
66 thickness regime for cryo-ET.

67
68 In this work, we used cryo-FIB milling and cryo-ET for the three-dimensional (3D) visualization of *E. coli*
69 septa and the sPG layer with unprecedented detail, revealing several new ultrastructural features.
70 Micrographs of wild-type cells showed that constriction of the IM and OM was well coordinated at the start
71 of division, but that the distance between the membranes grew in cells at later stages of division due to
72 much deeper invagination of the IM. Live-cell imaging with fluorescent markers for the IM and OM showed

73 that this change in morphology arises from a more rapid constriction of the IM relative to the OM.
74 Importantly, mutants impaired for sPG synthesis maintained coordination between IM and OM invagination
75 throughout the division process and had division site architectures that resembled the shallowly constricted
76 ultrastructure of *C. crescentus*. Moreover, mutants defective for sPG remodeling were shown to be largely
77 blocked for OM constriction and their septa as well as those of wild-type cells were found to contain lateral
78 bridge structures and separate parallel plates of sPG reminiscent of septa from *S. aureus*. In addition to
79 tracking IM and OM dynamics, we also monitored the rates of sPG synthesis and remodeling at the division
80 sites of the various mutants and correlated them with the rates of lateral wall biogenesis, division site
81 ultrastructure, and the shape of daughter cell poles. Our results revealed that cell wall degradation at the
82 division site plays a role in both the activation of sPG synthesis and Z-ring condensation, suggesting
83 communication between the PG synthesis machinery on one side of the membrane and the cytoskeleton
84 on the other. Furthermore, this analysis provided compelling evidence that the cell elongation and division
85 machineries are in competition for shared PG precursors and that the relative activities of the two systems
86 determines the shape of division site constrictions and the poles they form. Overall, our results highlight
87 the plasticity of the division system and how modulation of its cell wall synthesis and remodeling activities
88 can help generate the array of cell and polar morphologies observed in the bacterial domain.

89 Results

90

91 *In situ* architecture of the *E. coli* cell envelope at the division site

92 Most of the available images of the division site architecture in *E. coli* come from conventional EM
93 micrographs of fixed and stained cells²⁸. Although these images have given us a general idea of how the
94 cell envelope is remodeled during division to build the daughter cell poles, the division site ultrastructure
95 observed depended greatly on the fixation conditions used. Some treatments yielded division sites with a
96 uniformly constricted architecture, whereas others captured cells with a partial crosswall septum composed
97 of a fold of IM sandwiching a stretch of sPG from which the OM was excluded^{15,29}. In contrast, whole-cell
98 cryo-ET images of *E. coli* grown in nutrient poor conditions to reduce their size have thus far only shown
99 uniformly constricted septa without a clear view of the sPG layer¹⁷. The variation in septal architecture
100 based on the imaging method or fixation condition used has made it difficult to draw definitive conclusions
101 about which architecture represents the native state of the division site. We therefore reinvestigated the
102 ultrastructure of the *E. coli* division site using cryo-FIB milling to obtain thin (~150-200 nm thick) lamellae
103 of dividing cells for subsequent *in situ* cryo-ET imaging (**Fig. S1**). A total of 9 tilt-series of wild-type cells
104 were acquired, aligned, and 3D reconstructed (**Table S1**). Additionally, to gain better visualization of sPG,
105 non-linear anisotropic diffusion (NAD) filtering was applied to denoise the cryo-electron tomograms. Using
106 the measured distance between the leading edge of the IM constriction for each image, they were grouped
107 into three classes representing what appeared to be different stages of division: (i) constriction, (ii)
108 septation, or (iii) cytokinesis (**Fig. 1A**). Cells with an IM-IM distance of around 500 nm were classified as
109 being in the constriction phase. They had a V-shaped constriction with a relatively uniform invagination of
110 the two membranes and an indented mesh of PG (**Fig. 1A-B, and S2A**). The second category of cells had
111 a much smaller IM-IM distance (50 nm). They displayed a partial septum in which the IM was observed to
112 be more deeply invaginated than the OM with an average difference of 134.1 (\pm 21) nm (mean \pm SD) in
113 their measured OM-OM versus IM-IM distance (**Fig. 1A-B, and S2B**). Strikingly, the denoised tomograms
114 showed an elongated, triangular wedge of PG filling the gap between the two membranes (**Fig. 1B**). This
115 structure is reminiscent of the lateral bridge in *S. aureus* septa connecting the plates of sPG¹⁰, except in
116 this case a network of electron densities is visible connecting the two plates of PG that will become the
117 daughter cell polar PG caps. In cells at the final stage of cytokinesis, IM fission was observed to be
118 completed, leaving cells connected by the two interwoven sPG plates. The OM of these cells displayed
119 deep constrictions with the leading edge of the membrane pointing between the two sPG plates,
120 presumably poised to traverse the remaining OM-OM distance of 100-250 nm to complete division (**Fig.**
121 **1A-B, S2C and Video S1**). No OM blebs or cytoplasmic mesosome-like structures were observed at the
122 division site in the cryo-ET data like those observed previously by conventional EM^{15,28}.

123

124 The different division site architectures observed in the cryo-ET analysis suggested that the constriction
125 rate of the IM exceeds that of the OM during division to promote the formation of the partial septa. To
126 investigate this possibility, we followed the constriction dynamics of each membrane using live-cell
127 fluorescence microscopy. The IM was tracked using a superfolder GFP (sfGFP) fusion to the IM-anchored
128 division protein ZipA (ZipA-sfGFP) whereas constriction of the OM was followed using mCherry fused to
129 the OM-localized lipoprotein Pal (Pal-mCherry) (**Fig. 1C and Video S2**). Analyzing the distribution of the
130 fluorescence signals of Pal-mCherry and ZipA-sfGFP at the division site confirmed the further constriction
131 of IM with respect to the OM (**Fig. 1D**) as seen by cryo-ET (**Fig. 1A-B**). Following time-lapse imaging of a
132 large population of cells ($N = 150$), the invagination rate of each membrane was calculated from
133 kymographs (**Fig. 1E-F**). We found that the IM constricted at a rate of 64.26 ± 33.98 nm/min and the OM
134 at a rate of 55.03 ± 23.25 nm/min. These results are in-line with previously measurements of cytokinesis
135 rates^{30,31}. Multiplying the difference in constriction velocity between the membranes by the average time
136 for cytokinesis (16.36 ± 7.49 min) predicts that the IM-IM versus OM-OM diameters will differ by upwards
137 of 147 nm at late stages in cell division, which is in good agreement with our cryo-ET data (**Fig. S2**). Thus,
138 the combined cryo-ET and time-lapse analysis definitively establish that *E. coli* divides by a mixed
139 constriction/septation mechanism. At early stages in the process, invagination of the three envelope layers
140 is well-coordinated, resulting in a V-shaped constriction architecture. However, because the IM invaginates
141 about 9 nm/min more rapidly than the OM, the distance between the two membranes grows as division
142 progresses and a partial septum with a structure of sPG reminiscent of some Gram-positive bacteria is
143 formed. Thus, the division site architectures of diverse bacteria appear to share more similarities than
144 previously anticipated.

145

146 **sPG synthesis and remodeling activities of the divisome define division site architecture**

147 We next wanted to determine how the architecture of the division site and the dynamics of its constriction
148 are altered by mutations affecting sPG synthesis and remodeling. The essential PG synthase of the
149 divisome is formed by a complex between FtsW and FtsI (FtsWI) (Taguchi et al., 2019). Following Z-ring
150 assembly at the prospective division site, a regulatory pathway is thought to be initiated that ultimately
151 results in the activation of sPG synthesis by this synthase³⁴⁻³⁷ (**Fig. 2A**). Activation is mediated in part via
152 a direct interaction between FtsWI and the FtsQ-FtsL-FtsB (FtsQLB) complex³⁸. Although the mechanism
153 is unclear, genetic evidence suggests that the FtsQLB activation event is stimulated by an essential peptide
154 within the division protein FtsN³⁹. Another domain of FtsN called the SPOR domain is responsible for
155 concentrating the activation peptide at the division site through its ability to bind sPG that has been
156 processed by PG cleaving enzymes called amidases³⁹⁻⁴¹. The amidases remove the stem peptides from
157 the glycan strands as they split the sPG septum to promote OM constriction and daughter cell separation⁴².
158 In the process, they generate the denuded PG glycan strands recognized by the SPOR domain^{40,41}. The
159 interplay between the activation of sPG synthesis by FtsN with amidase processing of sPG promoting the

160 recruitment of more FtsN to the division site has been proposed to generate a positive feedback loop, the
161 sPG loop, that drives the activation of sPG biogenesis and cell division³⁹. To modulate this process for our
162 analysis, we employed several different mutant strains (**Table S2-S3**): (i) a mutant lacking the SPOR
163 domain of FtsN (*ftsN-ΔSPOR*), (ii) mutants defective for one (*ΔenvC*) or both (*ΔenvC ΔnlpD*) activators
164 required for amidase activity⁴³, and (iii) a mutant (*ftsL**) encoding a variant of FtsL that hyperactivates sPG
165 synthesis by FtsWI and bypasses the requirement for FtsN³⁷ (**Fig. 2A**). A comprehensive gallery of cryo-
166 electron tomograms containing the analyzed *E. coli* strains is provided (**Fig. S3**). A total of 60 tomograms
167 were obtained and analyzed in this study (**Table S1**).

168

169 Division sites from cells deleted for the SPOR domain of FtsN resembled those observed previously for *C.*
170 *crescentus*¹⁶ (**Fig. 2B**). By cryo-ET, there appeared to be greater coordination between IM and OM
171 constriction throughout the division process with the IM-OM spacing in deeply constricted cells (79.2 ± 21.7
172 nm) measuring nearly half that of wild-type cells in the septation phase (**Fig. 2B, S2-3, Video S3**).
173 Fluorescence microscopy tracking of IM and OM constriction dynamics confirmed that the rate of
174 constriction for the two membranes was nearly identical in the *ftsN-ΔSPOR* mutant (**Fig. 2C-D, Video S2**).
175 In this case, the rate of IM constriction was reduced compared to wild-type cells (49.56 ± 13.93 versus
176 64.26 ± 33.98 nm/min) such that it more closely matched the rate of OM constriction (**Fig 2D**). As a result
177 of the close opposition of the IM and OM, the wedge of sPG observed in filtered tomograms was not as
178 elongated as in wild-type cells such that separate plates of material forming ahead of the wedge could not
179 be clearly visualized (**Fig. 2B**).

180

181 In contrast to the coordinated envelope constriction displayed by the *ftsN-ΔSPOR* mutant, cells defective
182 for both amidase activators (*ΔenvC ΔnlpD*) formed a Gram-positive-like septum in which the constriction
183 of the IM was completed without much observable invagination of the OM (IM-OM distance: $296.05 \pm$
184 133.45 nm in deeply constricted cells) (**Fig. 2B and S3**). A similar septal architecture was observed
185 previously for this mutant using conventional EM, but the ultrastructure of the sPG layer was not
186 preserved⁴⁴. NAD-filtering of the current cryo-electron tomograms revealed density corresponding to sPG
187 that was even more clearly discernable as two distinct plates of material than in the partial septa observed
188 in wild-type cells above (**Fig. 1B and 2B**). Furthermore, the tomograms also revealed a triangular wedge
189 of PG material at the outer edges of the septa that was not previously observed in the conventional EM
190 analysis and presumably serves as a roadblock to OM invagination (**Fig. 2B, Video S4**). It was not possible
191 to measure membrane constriction dynamics in live cells of the *ΔenvC ΔnlpD* double mutant due to its poor
192 growth. However, measurements in a mutant lacking only EnvC, the most important of the two amidase
193 activators⁴³, revealed a significant disparity between IM and OM constriction rates (**Fig. 2C-D, Video S2**).
194 Even though the IM constriction rate was slower than wild-type or *ftsN-ΔSPOR* cells (33.97 ± 18.42 nm/min)
195 the completion of IM invagination still preceded that of the OM by an average of 36.5 min (**Fig. S4**). Overall,

196 the results with the *ftsN*- Δ *SPOR* and amidase activation mutants indicate that impairing key components
197 of the divisome involved in sPG synthesis activation and remodeling alters the architecture of the *E. coli*
198 division site such that it begins to resemble that of other distantly related bacteria.

199

200 **Hyperactivated sPG biogenesis leads to aberrant division site architecture**

201 To determine the effects of hyperactivated sPG biogenesis on division site architecture, we imaged cells
202 of the *ftsL** mutant. Strikingly, cryo-ET revealed an altered architecture in which the density corresponding
203 to the wedge of sPG observed in wild-type and other mutant cells was missing, and the envelope at the
204 leading edge of the invagination was 48% thinner than in wild-type (**Fig. 2B and Fig. S5B**). Conversely,
205 the envelope in the nascent polar regions adjacent to the leading edge of the invagination was 15 % thicker
206 in *ftsL** cells than in wild-type with the bulged areas appearing to contain more PG than normal (**Fig. S5B**
207 **and Video S5**). As expected from the faster division time measured previously for *ftsL** mutant³⁷, live-cell
208 imaging showed that the constriction velocity of the IM was much greater than for wild-type cells ($86.18 \pm$
209 33.12 nm versus 64.26 ± 33.98 nm/min) (**Fig. 2C-D, Video S2**). Surprisingly, the rate of OM constriction
210 was measured to be much slower than that of the IM (42.60 ± 18.49 nm versus 55.30 ± 23.25 nm) (**Fig.**
211 **2C-D**), a difference that would normally be expected to give rise to cells with partial septa with large
212 distances between the IM and OM. However, partial septa were not observed in the tomograms (**Fig. 2B**).
213 The distances between the IM and OM remained relatively constant in all the cells that were imaged (**Fig.**
214 **2B and Fig. S2-3**). This discrepancy is likely due to the PG binding activity of Pal causing the Pal-mCherry
215 OM reporter to get stuck in the thicker PG that accumulates behind the closing septum and therefore to
216 track poorly with the leading edge of the invaginating OM in these cells. In contrast, cryo-ET data directly
217 visualize OM. Notably, upon closer inspection of kymographs of the *ftsL** mutant, we noticed that one side
218 of the cell constricted much faster than the other (**Fig. 2C**), a phenomenon that was also observed by cryo-
219 ET (**Fig. S6A-C**). Applying Fourier filtering to kymographs allowed us to distinguish between forward and
220 reverse signal trajectories in order to compare the constriction velocity for each side of the division site and
221 assess the degree of anisotropy during septum closure. We found that *ftsL** showed a higher but not
222 statistically significant (Kruskal-Wallis ANOVA, $p = 0.056$) anisotropy score for both IM and OM constriction
223 compared to the other strains (**Fig. S6B-C**). Additionally, when cells were imaged in vertical orientation,
224 the constriction of *ftsL** cells was observed to be less circular than in wild-type as expected for uneven
225 closure of the division ring (**Fig. S6D**). Thus, circumvention of the normal controls regulating sPG
226 biogenesis in the *ftsL** mutant results in aberrant division site geometry and abnormal thickening of the
227 envelope at the cell poles. These cells also lack an observable sPG wedge, which may destabilize the
228 division site and help explain why these mutants were originally found to lyse at elevated temperatures^{45,46}.

229

230

231

232 **sPG degradation activates its synthesis**

233 To better understand the mechanism(s) by which the observed changes in division site architecture are
234 caused by mutations altering divisome components, we measured the rates of sPG synthesis and
235 degradation in *ftsL**, *ftsN-ΔSPOR*, and *ΔenvC* cells relative to those of wild-type using two different
236 cytological assays (**Fig. 3 and S7**). The first assay used a pair of compatibly labeled fluorescent D-amino
237 acids (FDAAs), YADA and HADA⁴⁷. In *E. coli*, these probes are primarily incorporated into the peptide
238 stem of PG by alternative crosslinking enzymes called L,D-transpeptidases (LDTs)⁴⁸. Because they do not
239 use the canonical PG synthases (e.g. FtsW, PBP1b, etc.) for incorporation, FDAAs only provide an indirect
240 readout of nascent PG synthesis. Nevertheless, when two probes are used for labeling in sequence, they
241 can accurately label areas of newly synthesized material⁴⁹. In our experiments, we grew cells for an
242 extended period in the presence of YADA to label the entire PG sacculus. A portion of these cultures was
243 then fixed to establish the YADA labeling baseline while other portions were washed, pulsed with HADA
244 for different lengths of time, and then fixed prior to visualization. The intensity of the HADA signal that
245 appeared at midcell after the pulses was used as a measure of the rate of sPG insertion (**Fig. 3A**).
246 Additionally, the YADA label was used to follow the fate of old PG with a comparison of the signal intensity
247 at midcell before and after the HADA pulse providing a measure of sPG degradation (**Fig. 3A**). To measure
248 nascent PG synthesis directly, the second assay employed a MurNAc-alkyne probe⁵⁰ in conjunction with
249 HADA (**Fig. S7**). In this case, cells were pre-labeled with HADA to mark old PG and pulsed with MurNAc-
250 alkyne, which is incorporated into the PG precursor lipid II and used directly by canonical synthases to
251 build new PG³⁰. Thus, using click chemistry and a clickable fluorescent dye, the rate of sPG insertion was
252 measured from the MurNAc-alkyne labeling intensity, and comparison of the HADA signal before and after
253 the pulse was used to determine the rate of sPG degradation.

254
255 Both PG biogenesis assays yielded qualitatively similar results (**Fig. 3 and S7**), and the measurements of
256 sPG synthesis correlated well with the rates of IM invagination determined above (**Fig. 2D**). The *ftsL**
257 mutant synthesized sPG faster than all other strains just as it had the fastest rate of IM invagination (**Fig.**
258 **2D, 3B, and S7D**). This result confirms that activated FtsQLB complexes indeed hyperactivate sPG
259 synthesis as suggested by their recently reported effects on the dynamic motions displayed by the FtsWI
260 PG synthase³⁰. Notably, the dual FFAA assay detected a significant amount of old PG at the division sites
261 prior to the HADA pulse, and this material appeared to be relatively stable during the time course.
262 Additionally, bright foci of old material were also observed at the poles of many cells after extended YADA
263 labeling (**Fig. 3B S8A-B**). This accumulation of old material likely corresponds to the thickened areas of
264 cell wall in the curved regions of septa and nascent poles observed by cryo-ET of the *ftsL** mutant (**Fig.**
265 **S5 and S8C-D**), reinforcing the conclusion that short-circuiting the normal controls governing the activation
266 of sPG biogenesis not only leads to more rapid sPG synthesis and septal closure, but also results in the
267 aberrant accumulation of PG within the developing cell poles.

268 As suggested by their slower than normal rates of IM invagination, both the *ftsN-ΔSPOR*, and *ΔenvC*
269 mutants displayed a reduced rate of sPG synthesis relative to wild-type cells (**Fig. 3C and S7D**). In the
270 MurNAc-alkyne assay, the *ftsN-ΔSPOR* mutant also showed a reduced septal labeling efficiency (**Fig.**
271 **S7C**), which is another indication of reduced sPG synthesis activity³⁰. Although the sPG synthesis rates
272 were similar, the two mutants differed greatly in their rates of sPG degradation. The *ftsN-ΔSPOR* mutant
273 displayed relatively normal rates of sPG degradation whereas *ΔenvC* cells showed reduced turnover of
274 sPG as expected for a mutant lacking an important amidase activator (**Fig. 3D-E and S7E**). The
275 combination of slower sPG synthesis with relatively normal sPG degradation explains the well-coordinated
276 constriction phenotype displayed by the *ftsN-ΔSPOR* mutant in the cryo-ET analysis. Although reduced
277 sPG degradation was expected for the amidase activation mutant based on its cell chaining phenotype
278 and abnormal septal morphology, it has not been directly demonstrated previously. The reduced rate of
279 sPG synthesis in the *ΔenvC* cells is notable, however, because it indicates that proper sPG processing by
280 the amidases is required for normal rates of sPG synthesis. This result along with the reduced rate of sPG
281 synthesis observed for the *ftsN-ΔSPOR* mutant provides strong support for the sPG loop model for PG
282 biogenesis during division, which so far has been based solely on inferences from a genetic analysis of
283 the domain functions of FtsN³⁹.

284 285 **sPG degradation is required for normal Z-ring formation**

286 In the FDAA labeling experiments we noticed that cells lacking EnvC commonly displayed closely spaced
287 sPG labeling consistent with the aberrant formation of adjacent division sites (**Fig. 4A**). Accordingly, closer
288 examination of the localization of Pal-mCherry in these cells revealed that double bands of the OM marker
289 for sites of cell constriction occurred at a significantly elevated frequency over wild-type or *ftsN-ΔSPOR*
290 cells (**Fig. 4B, E-F**). These double constrictions were typically observed within the cell body, but we also
291 observed constrictions near cell poles, generating what appeared to be minicells (**Fig. 4C, G**). However,
292 free minicells were not observed in the culture, suggesting that these aberrant poles were likely generated
293 from a double constriction event within the cell body, one of which was aborted while the other completed
294 division to leave behind a daughter with a polar constriction. Another defect in division we noticed in the
295 *ΔenvC* cells was the formation of membrane blebs emanating from some of the developing septa (**Fig.**
296 **4C**). Cells with such blebs were often observed to lyse, suggesting there was a catastrophic failure in
297 division. Lysed cells and double constrictions were also observed in the cryo-ET analysis of *ΔenvC ΔnlpD*
298 cells (**Fig. 4D**).

299
300 In addition to the aberrant sPG and Pal-mCherry localization, the pattern of ZipA-sfGFP was also altered
301 in the *ΔenvC* mutant relative to wild-type and the other mutants (**Fig. 4H, Video S6**). ZipA is an FtsZ-
302 binding protein and a marker for the Z-ring⁵¹. Many ZipA-sfGFP structures in cells lacking EnvC were
303 diffuse, suggesting that they are having difficulty condensing into the tight Z-ring structure typical of normal

304 cells (**Fig. 4H**). Consistent with this possibility, averaging the ZipA-sfGFP signals for a population of cells
305 (N = 100) either over a 10-minute time window or over a 2 μ m volume spanning midcell showed that the
306 fluorescent signal was more broadly distributed in the $\Delta envC$ mutant than in wild-type cells or cells of the
307 other mutants (**Fig. 4I-J**). Notably, this phenotype was not suppressed by combining the sPG synthesis
308 activating *ftsL** mutation with $\Delta envC$, indicating that it likely stems from the loss of sPG processing not its
309 collateral effect on sPG synthesis (**Fig. 4H-J**). A similar diffusion of the Z-ring signal has been observed
310 for cells defective for FtsZ-binding proteins like ZapA that are thought to bundle FtsZ polymers to condense
311 the ring^{52,53}. These results therefore suggest a previously unappreciated role for sPG hydrolysis by the
312 amidases in the periplasm in promoting Z-ring condensation in the cytoplasm. The observation of double
313 septa and failed division sites also indicates an unexpected role for amidase activation in division site
314 stability and/or placement in addition to their known function in cell separation (see Discussion).

315

316 **Competition between elongation and sPG biogenesis determines polar shape**

317 The idea that the cell elongation and division machineries might be in competition with one another was
318 proposed many years ago^{54,55}. However, experimental support for such a competition has been limited,
319 and it has never been demonstrated that competition occurs at the level of PG biogenesis. To investigate
320 this possibility further, we took advantage of the PG labeling assays used to measure sPG biogenesis to
321 also quantify the incorporation of new PG material into the sidewall (cell cylinder) during the MurNAc-
322 alkyne or HADA pulses (**Fig. 3F and S7F**). Importantly, we found that sidewall PG and sPG synthesis were
323 inversely proportional in the different strains we studied. Sidewall PG incorporation was highest in the *ftsN*-
324 $\Delta SPOR$ mutant, which had one of the lowest rates of sPG synthesis (**Fig. 3 and S7**). Conversely, sidewall
325 PG synthesis was the lowest in the *ftsL** mutant that displayed the highest measured rates of sPG
326 production (**Fig. 3 and S7**). In addition to the rates of sidewall PG biogenesis being inversely proportional
327 to that of sPG biogenesis, they were also found to be directly related to the single cell elongation rates of
328 the division mutants, with *ftsN*- $\Delta SPOR$ mutants elongating 1.5 times faster than *ftsL** cells (**Fig. 5A**).
329 Another measure of cell elongation activity is the circumferential motions of MreB and other components
330 of the Rod complex around the cell cylinder⁵⁶⁻⁵⁸. We therefore tracked the motion of a mNeonGreen fusion
331 to MreB in wild-type and mutant cells using a combination of structured illumination microscopy and total
332 internal reflection fluorescence (SIM-TIRF) imaging. Consistent with the sPG synthesis measurements,
333 the total number of directionally moving MreB filaments per area was significantly reduced in *ftsL** and
334 $\Delta envC$ cells (**Fig. 5B-C, Video S7**). Interestingly, while loss-of-function mutations in the division machinery
335 (e.g., *ftsN*- $\Delta SPOR$, $\Delta envC$) result in an increased cell length, hyperactivation of the division machinery
336 (e.g., *ftsL**) leads to shorter cells than wt (**Fig. S9A**). Concomitantly, mutants displaying reduced sidewall
337 PG incorporation rates and fewer directionally moving MreB filaments such as *ftsL** and $\Delta envC$, were also
338 found to display significantly increased cell width (**Fig. S9B**), which are indicative of reduced Rod complex
339 activity⁵⁹.

340 Notably, the observed interplay between cell elongation and division appeared to impact the geometry of
341 the division site and the shape of the daughter cell poles (**Fig. 5D**). The *ftsN-ΔSPOR* mutant which
342 elongates more rapidly and constricts slower, displayed an elongated division site area and a shallower
343 OM invagination angle at midcell as compared to wild-type cells (**Fig. 5D-G**). This altered constriction
344 geometry was also observable in the cryo-electron tomograms of dividing cells and correspondingly gave
345 rise to daughter cells with pointier poles than wild-type (**Fig. 5F, H**). On the other hand, the rapidly
346 constricting *ftsL** mutant formed daughters with relatively blunt cell poles (**Fig. 5F, H**).

347
348 We reasoned that the variation in division site and polar geometry among the different strains could be
349 related to the activity of the Rod complex at or near the division site. In this case, mutants that take longer
350 to complete the division process (such as *ftsN-ΔSPOR*) would allow for more elongation activity in the
351 curved cell region adjacent to the site of constriction, thereby generating shallower constrictions and
352 elongated poles (**Fig. 5E-G**). Conversely, mutants that divide rapidly (such as *ftsL**) would have less
353 opportunity to elongate the region around the division site and thus form steep constrictions and blunt
354 poles (**Fig. 5E-G**). To investigate this possibility, we quantified the number of directionally moving MreB
355 filaments in proximity (≤ 200 nm) to cell constrictions highlighted by Pal-mCherry foci at mid-cell (**Fig. 5B-**
356 **C, Video S7**). Directionally moving MreB filaments were readily observed to pass through division sites in
357 both early and late pre-divisional cells in all strains tested. Notably, however, the *ftsN-ΔSPOR* mutant
358 displayed more MreB tracks at the division site at late stages of division than all other strains, and the *ftsL**
359 mutant showed the least number of total MreB tracks at the division site (**Fig. 5C**). Thus, the density of
360 MreB tracks at the division site for these cells correlates well with the degree of constriction site and cell
361 pole elongation observed for the different strains. The outlier was the $\Delta envC$ mutant, which had an inverted
362 trend of having fewer directionally moving MreB tracks at early division stages than at later points (**Fig.**
363 **5C**). We suspect that this change is due to the defect in sPG splitting, which causes a steep curvature of
364 the inner membrane at early points in division that is likely to be unfavorable for MreB localization^{60,61}.
365 However, at later stages when sPG processing eventually allows for slow constriction of the OM, this
366 curvature likely becomes more favorable for MreB localization allowing elongation to occur near the
367 division site to generate a shallow constriction like that of the *ftsN-ΔSPOR* mutant. Overall, these results
368 not only provide strong support for a competition between the PG biosynthetic machineries involved in cell
369 elongation and division, but they also highlight the potential for this competition to define the morphology
370 of the daughter cell poles.

371 **Discussion**

372

373 Understanding the mechanisms regulating bacterial division requires unambiguous visualization of the
374 native cell envelope architecture at division sites. Previously obtained data from EM^{28,62}, CEMOVIS^{63,64}
375 and cryo-ET^{17,65} of Gram-negative bacteria, lacked a clear view of the sPG material produced by the
376 division machinery. Here, we overcome this limitation by combining cryo-FIB milling with cryo-ET to
377 visualize the division site of *E. coli*, providing 3D visualization of the *in situ* division site architecture at
378 nanometer resolution. Our data reveal several new ultrastructural features of the Gram-negative cell wall,
379 including a wedge-like formation of sPG that may play an important role in fortifying the septum against
380 osmotic rupture. Integrating these observations with dynamic measurements of sPG synthesis and
381 remodeling in several division mutants led to several new mechanistic insights into the process of cell
382 division and how its interplay with cell elongation can modulate cell shape (**Fig. 6**).

383

384 **Architecture of the sPG layer**

385 In tomograms of wild-type cells just starting to constrict, all three envelope layers appeared to be
386 invaginating in concert, and little change in the sPG relative to the sidewall PG was evident. However, cells
387 in advanced stages of division had an increased distance between the IM and OM and formed a partial
388 septum. In NAD-filtered tomograms of these cells, a triangular wedge of what is likely to be sPG is observed
389 at the lagging edge of the septum closest to the tip of the invaginating OM. The wedge thins as it
390 approaches the leading edge of the closing IM, and in this narrow portion of the septum, two dense tracks
391 of material are often discernable that correspond to the PG layers that will eventually fortify the daughter
392 cell poles. In cells defective for sPG processing by the amidases, the sPG wedge structure is more
393 prominent than in wild-type cells and it appears to impede the invagination of the OM. We thus infer that
394 amidases process this structure to allow constriction of the OM. Furthermore, because the sPG wedge is
395 observed in deeply constricted wild-type cells as well as unconstricted amidase activation mutants, we
396 suspect that the structure is dynamic with its lagging edge being degraded as new wedge material is
397 deposited at the leading edge. Such a spatial separation of synthesis and degradation would allow the
398 sPG wedge to move in a treadmill-like fashion ahead of the OM as the septum closes.

399

400 Premature separation of the daughter cell PG layers before a continuous wall structure is formed between
401 them would create a tear in the PG matrix and ultimately cause osmotic cell lysis. The positioning of the
402 sPG wedge at the lagging edge of the septum suggests that it might function to prevent such a catastrophe
403 by providing a buffer of extra PG material linking the daughter cells. Accordingly, the *ftsL** mutant lacks an
404 observable sPG wedge structure and has been shown to have a temperature-sensitive lysis phenotype^{45,46}.
405 We therefore conclude that the observed wedge structure plays a role in septal integrity similar to the
406 bridging portion of the π -like PG structure observed in dividing *S. aureus* cells¹⁰. However, the difference

407 is that the wedge is likely to be continuously remodeled as cells divide gradually whereas the bridge in *S.*
408 *aureus* appears to provide a static connection between daughter cells until the end of the division process
409 when lesions in the bridge are created and crack propagation results in extremely rapid cell separation⁶⁶.

410

411 The enzymes responsible for creating the sPG wedge remain to be identified, but our results with the *ftsL**
412 mutant suggest that it is not made by FtsWI synthase. This mutant is thought to hyperactivate FtsWI^{30,35–}
413 ³⁸. Therefore, if the wedge were produced by the FtsWI synthase, the *ftsL** mutant would be expected to
414 produce a thicker or otherwise larger wedge. Instead, it lacks a wedge altogether, suggesting that
415 enhanced FtsWI activity disrupts biogenesis of the sPG wedge by other synthases. An attractive candidate
416 for this additional synthase is the class A penicillin-binding protein (aPBP) PBP1b. Inactivation of PBP1b
417 has been found to be synthetically lethal with defects in FtsWI activation, and the affected mutants were
418 found to lyse due to septal lesions, suggesting that this aPBP promotes division site stability^{35,67}. The
419 location of the wedge at the lagging edge of the division site closest to the OM is also consistent with a
420 role for PBP1b in its construction given that this enzyme and related aPBPs require activation by
421 lipoproteins anchored in the OM to make PG^{68,69}. Thus, the outer fork of the division site where the wedge
422 is located is the only place where aPBPs would be predicted to be functional. Although further work will be
423 required to test this model, it provides an attractive explanation for the division of labor between the aPBP
424 and FtsWI synthases at the site of cell constriction, with the FtsWI synthase promoting ingrowth of the PG
425 layer and the aPBPs providing backfill to counter the activity of sPG remodeling enzymes, thereby
426 stabilizing the septum and preventing lysis.

427

428 **The sPG activation loop**

429 The proposal that FtsN and the amidase enzymes cooperate in a positive feedback loop that promotes
430 sPG synthesis is based on insightful reasoning aimed at explaining how the different domains of FtsN
431 might work together³⁹. However, this model lacks direct experimental support. A major prediction of the
432 model is that proper sPG synthesis should require both the SPOR domain of FtsN to recognize denuded
433 glycan strands at the division site and amidase activity to generate them³⁹. Our results indicate that this is
434 indeed the case. Both the *ftsN-ΔSPOR* mutant and a mutant defective for amidase activation were found
435 to synthesize sPG at a reduced rate compared to wild-type cells. Notably, sPG is still made in these
436 mutants, and even cells defective for all amidases or amidase activators can complete septum formation
437 in *E. coli*. In the case of the *ftsN-ΔSPOR* mutant, other SPOR domain containing division proteins like
438 DedD are likely to be promoting feedback loops analogous to that of FtsN⁷⁰. However, the observation that
439 mutants defective for all cell division amidases still make septa suggests that although efficient sPG
440 biogenesis depends on the sPG loop, it is not absolutely required to make sPG.

441

442 In addition to stimulating sPG synthesis, the sPG activation pathway in which the sPG loop operates also
443 appears to be important for normal septal architecture. The *ftsL** mutant hyperactivates the FtsWI synthase
444 and eliminates the strict FtsN requirement for sPG biogenesis³⁷. This short-circuiting of the normal division
445 activation pathway not only causes the loss of the sPG wedge structure observed in wild-type and other
446 mutant cells, but it also promotes the aberrant accumulation of PG within the developing cell poles.
447 Whether this accumulation results from inappropriate activation of PG synthesis by FtsWI or PBP1b, the
448 improper turnover of the deposited material, or some combination of the two remains unknown.
449 Nevertheless, what is clear is that bypassing the normal controls involved in sPG activation and speeding
450 up the process has adverse consequences on the envelope architecture of the poles that are formed. We
451 therefore infer that the normal divisome activation pathway serves an important function in coordinating
452 different activities of the machinery to ensure that division is successfully completed once it is initiated and
453 that the polar end products it produces have a uniform surface.

454

455 **PG hydrolysis and the Z-ring**

456 Over the years, many factors have been identified that help to position the Z-ring and condense it at midcell.
457 These proteins are typically thought to act upstream of divisome maturation and the activation of sPG
458 biogenesis⁶. However, our results have uncovered an unexpected connection between the activation of
459 sPG processing by the amidase and Z-ring structure, suggesting there is feedback to the Z-ring from events
460 downstream of sPG synthesis activation. Z-rings were found to be poorly condensed in mutant cells lacking
461 the amidase activator EnvC. Additionally, closely spaced constrictions or areas of sPG biogenesis were
462 also observed at an elevated frequency in these cells, suggesting that division sites are unstable and fail
463 before they complete the division process. Notably, closely spaced constrictions were also evident in prior
464 EM of chaining cells lacking all amidases⁴², and amidase activity has been shown to be critical for the
465 completion of cell constriction in the related Gram-negative bacterium *Pseudomonas aeruginosa*⁷¹. Taken
466 together, these results suggest the counterintuitive notion that sPG degradation by the amidases is
467 required to stabilize the divisome, most likely via a positive influence on the structure of the Z-ring that
468 promotes or maintains its condensation. Given that the amidases act on sPG in the periplasm, they are
469 unlikely to directly modulate FtsZ activity. Rather, their effect is probably mediated through SPOR domain
470 proteins like FtsN and DedD that bind the amidase processed glycans^{40,41}. These proteins have
471 transmembrane domains and N-terminal cytoplasmic tails, which in the case of FtsN is known to associate
472 with the FtsZ-binding protein FtsA^{72,73}. Thus, the status of sPG biogenesis in the periplasm could be
473 communicated to the Z-ring in the cytoplasm using the binding of SPOR domain proteins to denuded
474 glycans as a proxy. Whether the effect might be mediated simply by concentrating the cytoplasmic domains
475 of SPOR proteins at the division site to modulate the activity of FtsZ-binding proteins or via more complex
476 mechanisms requires further investigation, but the general picture that emerges is that the divisome

477 activation pathway is not a one-way street from Z-ring formation to sPG synthesis and processing. The Z-
478 ring is also likely to be receiving stabilizing/activating signals back from the PG biogenesis machinery.

479

480 **Cell shape and the balance between cell division and elongation**

481 The idea that the cell elongation and division machineries may be in competition with one another has
482 been discussed in the field for some time^{54,55}. However, it has only been recently that evidence for such a
483 completion has been presented. Cells with a temperature-sensitive allele of *ftsI* (*ftsI23*) were found to
484 elongate faster than wild-type during growth at the permissive temperature⁷⁴. Conversely, hyperactivated
485 for the Rod complex were found to be longer than a wild-type control, suggesting that division occurs less
486 frequently when cell elongation is stimulated⁷⁵. Finally, the overproduction of cell wall endopeptidases
487 implicated in cell elongation was found to cause lethal cell division defects in mutants impaired for FtsWI
488 activation⁶⁷. Although these findings are supportive of cell elongation occurring at the expense of division
489 and vice versa, it has remained unclear whether this competition occurs at the level of PG synthesis. Here,
490 we used three independent assays (NAM/FDAA incorporation, single-cell elongation rate, and MreB
491 tracking) to demonstrate that septal and side wall PG synthesis rates are inversely correlated to each
492 other, providing strong support for antagonism between the activities of the elongation and division
493 systems which most likely stems from a competition for the limited supply of the lipid II PG precursor.
494 Importantly, our results indicate that this competition does not just affect cell width or how long or short
495 cells are. It also influences the geometry of the septum and the shape of the daughter cell poles. Thus,
496 modulation of the relative activities of the elongation and division systems is likely to play an important role
497 in the generating the diversity of shapes observed among different bacteria.

498 **Acknowledgments**

499 We are grateful to Phat Vinh Dip, Edward Brignole and Anna Osheroov at the MIT.nano cryo-EM facility and
500 KangKang Song and Chen Xu at the University of Massachusetts cryo-EM facility for providing access to
501 the cryo-EM microscopes and for all their help, advice, and maintenance of cryo-EM equipment.
502 Furthermore, we would like to express our gratitude to the MicRoN imaging core at Harvard Medical
503 School, for excellent advice on live cell imaging and maintenance of fluorescence microscopes. We would
504 also like to thank Calixto Saenz and the Microfabrication Core facility at the department of Systems Biology
505 at Harvard Medical School, for the micro-pillar design, fabrication, and consultations. Lastly, we are grateful
506 to Thomas Bartlett and Erkin Kuru for advice and helpful discussions on FDAA and NAM labeling
507 experiments. P.P.N. was supported by the Swiss National Science Foundation (SNF) with both Early
508 Postdoc.Mobility P2BSP3_188112 and Postdoc.Mobility fellowships P400PB_199252. A.V. was supported
509 by a EMBO long-term postdoctoral fellowship ALTF_89-2019 and a SNF Postdoc.Mobility fellowship
510 P500PB_203143. C.A. is funded by Charles University with a PRIMUS grant (PRIMUS/20/SCI/015). This
511 work was also supported by funding from the National Institutes of Health (R35GM142553 to L.H.C. and
512 R01AI083365 to T.G.B.) and Investigator funds from the Howard Hughes Medical Institute (T.G.B.).

513

514 **Author Contributions**

515 P.P.N and A.V. conceived the project, performed experiments, and analyzed and interpreted the data.
516 P.P.N performed cryo-FIB / cryo-ET and image processing. A.V. generated mutants and performed
517 fluorescence microscopy experiments. V.Y.A. performed 3D segmentations of cryo-ET data. P.M.L.
518 established SIM-TIRF workflow and assisted in data collection. C.A. contributed to cell morphology
519 analyses. L.H.C and T.G.B provided infrastructure and scientific advice. P.P.N, A.V., L.H.C. and T.G.B.
520 wrote the manuscript with input from all authors.

521

522 **Declaration of Interests**

523 The authors declare that there are no competing financial interests.

524

METHODS

525 Media, bacterial strains, and mutagenesis

526 Indicated strain derivatives of *E. coli* MG1655 used in this study are listed in Table S2-S3. Bacteria were
527 grown in LB (1% Tryptone, 0.5% yeast extract, 0.5% NaCl) or M9 medium⁷⁶ supplemented with 0.2% D-
528 glucose and casamino acids. For selection, antibiotics were used at 10 $\mu\text{g ml}^{-1}$ (tetracycline), 25 $\mu\text{g ml}^{-1}$
529 (chloramphenicol), and 50 (kanamycin, ampicillin) $\mu\text{g ml}^{-1}$. Mutant alleles were moved between strains
530 using phage P1 transduction. If necessary, the antibiotic cassette was removed using FLP recombinase
531 expressed from pCP20⁷⁷. All mutagenesis procedures were confirmed by PCR.

532

533 Cryo-EM specimen preparation

534 Figure S1 summarizes the cryo-FIB / cryo-ET pipeline utilized in this study. Bacterial strains were grown
535 overnight in LB media, back diluted 1:1000 and incubated shaking at 37°C, 250 rpm to $\text{OD}_{600} = 0.3$. Cells
536 were harvested by centrifugation (2 min, 5000 x g, RT) and resuspended in LB media to a final $\text{OD}_{600} =$
537 0.6. Three μL of cell culture were applied to Cflat-2/1 200 mesh copper or gold grids (Electron Microscopy
538 Sciences) glow discharged for 30 seconds at 15 mA. Grids were plunge-frozen in liquid ethane⁷⁸ with a
539 FEI Vitrobot Mark IV (Thermo Fisher Scientific) at RT, 100% humidity with a waiting time of 10 seconds,
540 one-side blotting time of 13 seconds and blotting force of 10. Customized parafilm sheets were used for
541 one-side blotting. All subsequent grid handling and transfers were performed in liquid nitrogen. Grids were
542 clipped onto cryo-FIB autogrids (Thermo Fisher Scientific).

543

544 Cryo-FIB milling

545 Grids were loaded in Aquilos 2 Cryo-FIB (Thermo Fisher Scientific). Specimen was sputter coated inside
546 the cryo-FIB chamber with inorganic platinum, and an integrated gas injection system (GIS) was used to
547 deposit an organometallic platinum layer to protect the specimen surface and avoid uneven thinning of
548 cells. Cryo-FIB milling was performed on the specimen using two rectangular patterns to mill top and
549 bottom parts of cells, and two extra rectangular patterns were used to create micro-expansion joints to
550 improve lamellae instability⁷⁹. Cryo-FIB milling was performed at a nominal tilt angle of 14°-18° which
551 translates into a milling angle of 7°-11°⁸⁰. Cryo-FIB milling was performed in several steps of decreasing
552 ion beam currents ranging from 0.5 nA to 10 pA and decreasing thickness to obtain 100-200 nm lamellae.

553

554 Cryo-electron tomography

555 All imaging was done on a FEI Titan Krios (Thermo Fisher Scientific) transmission electron microscope
556 operated at 300KeV equipped with a Gatan BioQuantum K3 energy filter (20 eV zero-loss filtering) and a
557 Gatan K3 direct electron detector. Prior to data acquisition, a full K3 gain reference was acquired, and ZLP
558 and BioQuantum energy filter were finely tuned. The nominal magnification for data collection was of
559 42,000x or 33,000x, giving a calibrated 4K pixel size of 2.193 Å and 2.565/2.758 Å, respectively. Data

560 collection was performed in the nanoprobe mode using the SerialEM⁸¹ or Thermo Scientific Tomography
561 5.3 software. The tilt range varied depending on the lamella, but generally was from -70° to 70° in 2° steps
562 following the dose-symmetric tilt scheme⁸². Tilt images were acquired as 8K x 11K super-resolution movies
563 of 4-8 frames with a set dose rate of 1.5-3 e-/Å²/sec. Tilt series were collected at a range of nominal defoci
564 between -3.5 and -5.0 μm and a target total dose of 80 to 180 e-/Å² (Table S1).

565

566 Cryo-electron tomography image processing

567 Acquired tilted super-resolution movies were motion corrected and Fourier cropped to 4K x 5K stacks,
568 minimizing aliasing effects using *framealign* from IMOD⁸³. Tilt series were aligned using *etomo* in IMOD⁸⁴
569 and *Dynamo*. CTF-estimation was performed in IMOD and/or using customized MATLAB scripts. CTF-
570 correction was performed by *ctfphaseflip* program in IMOD⁸⁵. CTF-corrected unbinned tomograms were
571 reconstructed by weighted back projection with and without a SIRT-like filter and subsequently 2x, 4x and
572 8x binned in IMOD⁸⁴.

573 Bandpass filtering and summed projection of cryo-tomogram slices was performed in *Dynamo*⁸⁶⁻⁸⁹
574 complemented with customized MATLAB scripts. Gaussian and NAD-filtering were performed in Amira
575 (Thermo Fisher Scientific) for visualization purposes. NAD-filtering was applied using the command
576 'Anisotropic Diffusion' in 3D mode for 5 iterations. Gaussian filtering was done by applying the command
577 'Gaussian Filter' under 3D mode with a Kernel size factor of 3. Whole 3D volume FFT filtering was
578 performed in IMOD.

579 Three-dimensional pole curvature rendering was performed in Amira by applying the commands
580 'Curvature' based on the triangulated 3D mesh and 'Shape Index' as implemented in Amira⁹⁰. Shape index
581 (SI) computes the surface scalar field which values are equal to

$$582 \quad SI = \frac{\pi}{2} \operatorname{atan} \frac{C_1 + C_2}{C_1 - C_2}$$

583 where C_1 and C_2 are the two principal curvatures. Shape index ranges from -1 to 1, negative values indicate
584 negative curvature, positive values indicate positive curvature and values close to 0 indicates flatness of
585 the surface⁹⁰ (Fig. 5).

586

587 Quantification of cryo-ET data

588 *Division site dimensions*

589 Summed projection images of cryo-ET tomograms were used to measure cell dimensions at the division
590 site. Measurements were performed in Fiji⁹¹ using the 'point to point' measuring tool. Measurements were
591 from IM to IM and from OM-OM. Descriptive statistics indicating N and mean ± SEM can be found in Fig.
592 S2.

593 *Periplasmic space*

594 Measurements of periplasmic space thickness were performed from OM to IM in the cell areas referred to
595 here as 'side wall', 'pole' and 'curve'. Measurements from IM to IM were performed in the cell area defined
596 in this study as septum (S5 and S8). We used a customized macro in Fiji that measures thirty Euclidean
597 distances from surface-to-surface areas in nm, e.g., from IM to IM at the septum. For these thirty single
598 measurements the mean was calculated, yielding a final single mean value per defined subcellular
599 localization, e.g., septum.

600

601 Sample preparation for live cell imaging

602 Overnight cultures of indicated *E. coli* strains were grown in LB supplemented with appropriate antibiotics
603 at 37°C. The next day, cells were harvested by centrifugation (2 min, 5000 x g, RT) and washed 2x with
604 M9 medium. Day cultures were back diluted (1:1000) and grown in M9 (0.2 % D-glucose, casamino acids)
605 supplemented with 50 µM IPTG and appropriate antibiotics at 30°C until OD₆₀₀ = 0.2 - 0.4. Cells were
606 harvested (2 min, 5000 x g, RT) and resuspended in 1/10th of the original volume. Two microliters of this
607 cell suspension were added onto a 1 % (w/v) agarose in M9 (0.2 % D-glucose, casamino acids) pad
608 supplemented with 50 µM IPTG and covered with a #1.5 coverslip.

609

610 Live cell imaging

611 All samples were imaged on a Nikon Ti-E inverted widefield microscope equipped with a fully motorized
612 stage and perfect focus system. Images were acquired using a 1.45 NA Plan Apo 100x Ph3 DM objective
613 lens with Cargille Type 37 immersion oil. Fluorescence was excited using a Lumencore SpectraX LED light
614 engine and filtered using ET-GFP (Chroma #49002) and ET-mCherry (Chroma #49008) filter sets. Images
615 were recorded on an Andor Zyla 4.2 Plus sCMOS camera (65 nm pixel size) using Nikon Elements (v5.10)
616 acquisition software. For subsequent deconvolution procedures, three 200 nm spaced Z-planes were
617 acquired for both fluorescence channels using 100% LED output power and 50 ms exposure. Temperature
618 was maintained at 30°C using a custom-made environmental enclosure. After a 20 min acclimatization
619 period, cells were imaged at a 2.5 min acquisition frame rate for a total observation time of 1-4 h.

620

621 Image processing for fluorescence microscopy

622 First, time-lapse series and Z-stacks were drift corrected using a customized StackReg plugin in Fiji^{91,92}.
623 Subsequently, fluorescence images were deconvolved using the classical maximum likelihood estimation
624 (CMLE) algorithm in Huygens Essential v19.10 (SVI) employing an experimentally derived PSF from 100
625 nm TetraSpeck beads (ThermoFisher). Image reconstruction was performed over 50 iterations with a
626 quality threshold of 0.01 and a signal-to-noise ratio set to 20 for live-cell imaging and 40 for fluorescent cell
627 wall probes in fixed samples. Chromatic aberrations between different fluorescent wavelengths were post-
628 corrected using the Chromatic Aberration Corrector in Huygens from TetraSpeck bead template. The same
629 image reconstruction parameters and chromatic aberration templates were applied to images which were

630 compared to each other. Last, reconstructed fluorescence images were merged back to phase contrast
631 images and rendered for figure or movie display with Fiji.

632

633 Measuring cell envelope constriction dynamics

634 Fluorescent fusions to IM anchored protein ZipA, and OM lipoprotein Pal, allowed us to determine the
635 respective position of the different cell envelope layers during division. Constriction dynamics of IM and
636 OM were derived from kymographs generated using the Fiji plugin *KymographClear*⁹³ and automatically
637 split into forward and reverse trajectories using Fourier filtering. This filtering step allows us to measure
638 the constriction rate for each side independently. Constriction kinetics were derived by automatically
639 extracting the fluorescent trajectories for ZipA and Pal using *KymographDirect*⁹³. Anisotropy of the division
640 process was determined by taking the ratio of the constriction velocity between the forward and reverse
641 trajectory. Only cells where the division site displayed no signs of displacement except for constriction
642 were analyzed to eliminate confounding effects on the analysis by excessive cell movement (e.g., pushing).

643

644 Measuring division site circularity of vertically imaged cells

645 For vertical imaging of bacterial cells undergoing division, similar procedures as described previously^{94,95}
646 were applied. Briefly, a silicon wafer containing 5.5 μm long and 1.5 μm wide photo-resist pillars was
647 generated following high aspect ratio photolithography procedures with an adhesion layer. The dimension
648 of these pillars reaches the practically feasible aspect ratio for photolithography designs and thus impedes
649 increasing pillar length without concomitantly increasing width, precluding elongated or chaining division
650 mutants. A modified silanization surface treatment with plasma cleaning was applied to increase the
651 surface hydrophobicity of the silicon wafer to minimize agarose accumulation. Agarose micro holes were
652 generated by pouring degassed 6 % agarose (w/v) in H_2O on the silicon wafer. Agarose was allowed to
653 solidify for 40 min at RT and was peeled off, cut into 5 x 5 mm pieces, and incubated in M9 medium
654 supplemented with 0.2 % D-glucose, casamino acids, 25 $\mu\text{g ml}^{-1}$ chloramphenicol and 50 $\mu\text{g ml}^{-1}$ ampicillin
655 overnight.

656

657 Cells were grown as described for sample preparation for live-cell imaging added on agarose pads. Cells
658 which were not trapped in micro holes were washed off gently using 1 ml of growth medium. Five
659 micrometer spanning Z-stacks (at a 200 nm step size) were acquired and subsequently deconvolved.

660

661 Circularity quantification was carried using the software package *Morphometrics*⁹⁶. Fluorescence signals
662 were segmented using Laplacian algorithm in combination the peripheral fluorescence setting. Circularity
663 (C) is calculated in *Morphometrics* as:

664

$$C = \frac{P^2}{4\pi \times A^2}$$

665 where (P) is the perimeter and (A) is the area enclosed by the circle and is a dimensionless measure. A
666 perfect circle displays a circularity of 1, while increasing values correspond to less circular objects.

667

668 Measuring Z-ring condensation from time-lapse data.

669 Condensation of cytoskeletal elements was addressed using similar procedures described by Squyres et
670 al., 2021. Briefly, five frames (corresponding to 10 min) from recorded time-lapse series were sum-
671 projected in Fiji. Z-rings in these sum projection images were then aligned along the length axis and
672 average-intensity projected into single image. Fluorescence intensity was measured across the full width
673 along horizontal axis of the averaged projection image. Intensity values were normalized and their
674 corresponding FWHM values were calculated in MATLAB.

675

676 Measuring Z-ring condensation from 3D data.

677 Similar procedures as outline for measuring Z-ring condensation in time-lapse series were applied. Two
678 micrometer spanning Z-stacks (at a 200 nm step size) were acquired to capture a full three-dimensional
679 view of a cell. Images were restored in Huygens as described above. Image volumes were sum-projected
680 into a single plane, Z-rings extracted, aligned, and averaged described above. Fluorescence intensity
681 profiles were measured identically as for time-lapse data. Snapshots for three-dimensional maximum
682 intensity projections were rendered in Huygens.

683

684 Measuring cell wall synthesis rates by biorthogonal NAM probes.

685 Septal cell wall synthesis rates were measured as described previously here^{98,99}. NAM-Alkyne was
686 purchased as a custom synthesis product from Tocris following the procedures of Liang et al., 2017. All
687 experiments were carried out in $\Delta murQ$ background and in presence of pCF436¹⁰⁰ for IPTG inducible
688 expression of AmgK and MurU. Overnight cultures were back diluted 1:1000 into fresh LB containing 15
689 $\mu\text{g ml}^{-1}$ gentamycin. Cells were grown at 37°C until $\text{OD}_{600} = 0.4$. Subsequently, 1.5 ml of cells were
690 harvested (2 min, 5000 x g, RT) and resuspended in 300 μl LB containing 1 mM IPTG and 0.5 mM HADA
691 to label all cell wall material by FDAAs. Samples were incubated rotating at 37°C for 30 min. Endogenous
692 UDP-NAM production was inhibited by the addition of 200 $\mu\text{g ml}^{-1}$ fosfomycin. After 10 min incubation, cells
693 were washed twice in 1.5 ml LB, 1 mM IPTG, 200 $\mu\text{g ml}^{-1}$ fosfomycin. Next, cells were incubated for 15 min
694 in the presence of 0.2 % (w/v) NAM-Alkyne, 1 mM IPTG, 200 $\mu\text{g ml}^{-1}$ fosfomycin at 37°C. Cells were fixed
695 using ice-cold 70 % (w/v) ethanol for 20 min at 4°C. Next, cells pellets were washed 3x with 1x PBS.
696 Biorthogonal NAM-Alkyne probes were labeled by click chemistry using 5 μM of Alexa488 azide substrate
697 according to manufactures instruction. Samples were stored in 20 μl PBS at 4°C and imaged within 48 h
698 of labeling experiment.

699

700 Samples were imaged on Nikon Ti2-E inverted widefield microscope equipped with a Lumencor Spectra
701 III light engine, and Semrock dichroics (LED-CFP/YFP/mCherry-3X-A-000, LED-DA/FI/TR/Cy5/Cy7-5X-A-
702 000) and emission filters (FF01-432/36, FF01-515/30, FF01-544/24). Images were recorded using a 1.45
703 NA Plan Apo 100 x PH3 oil objective with Olympus Type F immersion oil and a pco.edge 4.2bi Back
704 Illuminated Cooled sCMOS camera using Nikon Elements 5.2.

705 One micrometer spanning Z-stacks (separated by 200 nm) were acquired and subsequently deconvolved
706 as described under image processing for fluorescence microscopy. Z-stacks were sum-projected using
707 Fiji. *De novo* septal PG synthesis was measured by integrating the fluorescence intensity of NAM-Alexa488
708 along the division site using the line tool (width = 3 pixels). Levels of cell wall hydrolysis were assessed by
709 measuring the overall reduction in HADA fluorescence as compared to baseline signal intensity derived
710 from fixing cells prior to NAM chase.

711
712 Measuring cell wall remodeling by FDAA incorporation.

713 For FDAA pulse chase experiments, cells grown overnight were back diluted 1:1000 in fresh LB and grown
714 until OD600 = 0.4 at 37°C. Subsequently, 1.5 ml of cells were harvested (2 min, 5000 x g, RT) and
715 resuspended in 300 µl LB containing 0.5 mM YADA. Samples were incubated rotating at 37°C for 40 min.
716 Cells were washed once in 1.5 ml LB and resuspended in 300 µl LB containing 0.5 mM HADA. Samples
717 were incubated at 37°C for either for 2 min, 4 min, and 8 min prior to immediate fixation with 70 % ethanol.
718 After fixation, cells were washed 3x in PBS, stored in the dark at 4°C and imaged within 48 h. The same
719 image acquisition and analyses procedures were carried out as described for NAM probes. In addition to
720 the division site, fluorescence intensities measurements were also performed along the side wall and polar
721 region of the cells.

722
723 Cell shape quantification analyses

724 Bacterial cells were segmented and analyzed from still phase contrast images or time-lapse series using
725 the software package *Morphometrics*⁹⁶. Results from *Morphometrics* were post-processed using
726 customized MATLAB scripts to exclude erroneously segmented cell debris in live image data based on
727 area. Cell width, length and pole angles per segmented cell were directly extracted from *Morphometrics*.
728 We obtained the invagination angle from both sides of the cell at the invagination site. The invagination
729 site is defined as the narrowest segment of the cell, e.g., lowest cell width value, that present negative
730 curvature on both sides of the cell body. The cell elongation (E) was determined by a customized MATLAB
731 script:

$$732 \quad E = L_i - L_0$$

733 where L is cell length, L_0 is the cell length in the first frame and $i = 1, \dots, I$, where I is the number of frames.
734 The elongation rate is the slope of the linear regression performed on the plotted elongation values over
735 time in Prism (GraphPad 9.0.0).

736 **SIM-TIRF Microscopy and MreB Tracking**

737 Samples were prepared as described for live-cell imaging. Cells were added to high precision # 1.5
738 coverslips (Marienfeld) and placed on a 1 % (w/v) agarose pad in M9 (0.2 % D-glucose, casamino acids)
739 and imaged at room temperature on a Nikon Ti-2 N-SIM microscope, equipped with N-SIM spatial light
740 modulator illuminator, TIRF Lun-F laser combiner with 488 and 561 nm laser lines, a N-SIM 488/561 dual
741 band dichroic mirror, SR HP Apo TIRF 100x 1.5 NA oil objective with automated correction collar and
742 Hamamatsu Orca Flash 4.0 camera attached to a Cairn Research Twimcam splitter with a ET525/50m or
743 a ET605/70m emission filter (for MreB-sw-mNeonGreen or Pal-mCherry fusion, respectively). The
744 refractive index of the immersion oil (1.512) (GE Healthcare) was optimized for MreB-sw-mNeonGreen
745 signal and corrected using the automated correction collar for the Pal-mCherry fusion. Alignment of the
746 488 and 561 lasers for SIM-TIRF and 3D-SIM and of the N-SIM optics and illumination was performed
747 before each experiment at the image plane. First, a 3 min time-lapse series (at 3 s acquisition frame rate)
748 in SIM-TIRF mode was collected using 20 % laser power with 100 ms exposure time to follow MreB-sw-
749 mNeonGreen dynamics. Then, a single slice of a 3D-SIM Pal-mCherry (40 % laser power, 100 ms
750 exposure) and a brightfield reference image was acquired. Raw fluorescence images were reconstructed
751 using Nikon Elements 5.11 acquisition Software with indicated settings: MreB illumination contrast 0.8,
752 noise suppression 0.3 and blur suppression 0.05; Pal illumination contrast 3.75, noise suppression 0.1 and
753 blur suppression 0.5. Only reconstructed images with a quality score ≥ 8 and passed SIMcheck quality
754 test¹⁰¹ were used for further analysis. Subsequently MreB time-lapse series was overlaid over the
755 reference channels in Fiji.

756
757 Particle tracking was performed in Fiji using the TrackMate v6.0.1 plugin¹⁰². MreB filaments were detected
758 using the LoG-detector with an estimated radius of 0.3 μm . Spurious spots were filtered using a quality
759 threshold of 50. Spots were linked using a Kalman filter with an initial search radius for 0.2 μm and search
760 radius for 0.1 μm . No frame gaps were allowed. Only Tracks consisting of ≥ 4 continuous spots (12 s) and
761 traveled less than 1 μm in total distance were kept for further analysis. To analyze the nature of the
762 displacement of each track, the mean square displacement (*MSD*) was calculated using the MATLAB class
763 *msdanalyzer*¹⁰³ following the equation:

$$764 \quad MSD(\tau) = 2dD\tau$$

765 where (*t*) is the delay time and (*D*) is the diffusion coefficient. Slopes (α) of the individual *MSD* curves were
766 extracted using the Log-log fit of the *MSD* and the delay time τ . As the maximum delay time 75 % of the
767 track length was used. Tracks with a R^2 for $\log [MSD]$ versus $\log [t]$ below 0.95 indicative of a poor fit to
768 the *MSD* curve were excluded from the analysis. MreB filaments engaged in active cell wall synthesis are
769 displaced by the enzymatic action of the enzymatic activities of RodA and PBP2b^{56–58} and thus its *MSD*
770 curves display slopes of $\alpha \approx 2$ indicative of a transported particle motion above the rate of Brownian
771 diffusion (Fig. S10B). MreB filaments in constricting cells, as determined by the presence of a Pal-mCherry

772 foci at the division site, were analyzed by fitting a 200 nm wide region of interest to the cell division site.
773 Directional MreB tracks were deemed to contribute to the elongation of the division site. Early and late
774 division stages were distinguished by the presence of two separated Pal foci or a continuous fluorescent
775 signal across the cell, respectively.

776
777 **Statistical analysis**

778 All data measurements were plotted and analyzed using GraphPad Prism 9 (Version 9.1.2). In general,
779 (log-) normal distribution was tested by using Shapiro-Wilk test, for comparisons of two groups, significance
780 was determined by two-tailed, unpaired Student's t test with Welch correction and F test for variance
781 analysis. One-way ANOVA test were used for comparison of more than two groups using the
782 recommended post-test for selected pairwise comparisons. All experiments were carried out at least with
783 3 independent biological replicates. P values less than 0.05 were considered statistically significant. Levels
784 of significance are indicated by * $p < 0.05$, ** $p < 0.01$, *** $p < 0.001$, **** $p < 0.0001$; ns, not significant.

785

786 References

- 787 1. Silhavy, T. J., Kahne, D. & Walker, S. The bacterial cell envelope. *Cold Spring Harb. Perspect. Biol.*
788 **2**, a000414 (2010).
- 789 2. Konovalova, A., Kahne, D. E. & Silhavy, T. J. Outer Membrane Biogenesis. *Annu. Rev. Microbiol.* **71**,
790 539–556 (2017).
- 791 3. Rohs, P. D. A. & Bernhardt, T. G. Growth and Division of the Peptidoglycan Matrix. *Annu. Rev.*
792 *Microbiol.* (2021) doi:10.1146/annurev-micro-020518-120056.
- 793 4. Du, S. & Lutkenhaus, J. At the Heart of Bacterial Cytokinesis: The Z Ring. *Trends Microbiol.* **27**, 781–
794 791 (2019).
- 795 5. Mahone, C. R. & Goley, E. D. Bacterial cell division at a glance. *J. Cell Sci.* **133**, (2020).
- 796 6. Adams, D. W. & Errington, J. Bacterial cell division: assembly, maintenance and disassembly of the
797 Z ring. *Nat. Rev. Microbiol.* **7**, 642–653 (2009).
- 798 7. Beveridge, T. J. Ultrastructure, Chemistry, and Function of the Bacterial Wall. in *International Review*
799 *of Cytology* (eds. Bourne, G. H., Danielli, J. F. & Jeon, K. W.) vol. 72 229–317 (Academic Press,
800 1981).
- 801 8. Erickson, H. P. How bacterial cell division might cheat turgor pressure – a unified mechanism of
802 septal division in Gram-positive and Gram-negative bacteria. *BioEssays* **39**, 1700045 (2017).
- 803 9. Matias, V. R. F. & Beveridge, T. J. Native Cell Wall Organization Shown by Cryo-Electron
804 Microscopy Confirms the Existence of a Periplasmic Space in *Staphylococcus aureus*. *J. Bacteriol.*
805 **188**, 1011–1021 (2006).
- 806 10. Matias, V. R. F. & Beveridge, T. J. Cryo-electron microscopy of cell division in *Staphylococcus*
807 *aureus* reveals a mid-zone between nascent cross walls. *Mol. Microbiol.* **64**, 195–206 (2007).
- 808 11. Khanna, K. *et al.* The molecular architecture of engulfment during *Bacillus subtilis* sporulation. *eLife*
809 **8**, e45257 (2019).
- 810 12. Khanna, K., Lopez-Garrido, J., Sugie, J., Pogliano, K. & Villa, E. Asymmetric localization of the cell
811 division machinery during *Bacillus subtilis* sporulation. *eLife* **10**, e62204 (2021).
- 812 13. Lopez-Garrido, J. *et al.* Chromosome Translocation Inflates *Bacillus* Forespores and Impacts Cellular
813 Morphology. *Cell* **172**, 758–770.e14 (2018).
- 814 14. Nanninga, N., Koppes, L. J. H. & de Vries-Tijssen, F. C. The cell cycle of *Bacillus subtilis* as studied
815 by electron microscopy. *Arch. Microbiol.* **123**, 173–181 (1979).
- 816 15. Burdett, I. D. & Murray, R. G. Septum formation in *Escherichia coli*: characterization of septal
817 structure and the effects of antibiotics on cell division. *J. Bacteriol.* **119**, 303–324 (1974).
- 818 16. Judd, E. M. *et al.* Distinct Constrictive Processes, Separated in Time and Space, Divide *Caulobacter*
819 Inner and Outer Membranes. *J. Bacteriol.* **187**, 6874–6882 (2005).
- 820 17. Szwedziak, P., Wang, Q., Bharat, T. A. M., Tsim, M. & Löwe, J. Architecture of the ring formed by the
821 tubulin homologue FtsZ in bacterial cell division. *eLife* **3**, e04601 (2014).
- 822 18. Frank, J. *Electron Tomography: Methods for Three-Dimensional Visualization of Structures in the*
823 *Cell.* (Springer Science & Business Media, 2008).
- 824 19. Grimm, R., Typke, D., Bärmann, M. & Baumeister, W. Determination of the inelastic mean free path
825 in ice by examination of tilted vesicles and automated most probable loss imaging. *Ultramicroscopy*
826 **63**, 169–179 (1996).
- 827 20. Oikonomou, C. M. & Jensen, G. J. Cellular Electron Cryotomography: Toward Structural Biology In
828 Situ. *Annu. Rev. Biochem.* **86**, 873–896 (2017).
- 829 21. Hayles, M. F. *et al.* The making of frozen-hydrated, vitreous lamellas from cells for cryo-electron
830 microscopy. *J. Struct. Biol.* **172**, 180–190 (2010).
- 831 22. Marko, M., Hsieh, C., Schalek, R., Frank, J. & Mannella, C. Focused-ion-beam thinning of frozen-
832 hydrated biological specimens for cryo-electron microscopy. *Nat. Methods* **4**, 215–217 (2007).

- 833 23. Medeiros, J. M. *et al.* Robust workflow and instrumentation for cryo-focused ion beam milling of
834 samples for electron cryotomography. *Ultramicroscopy* **190**, 1–11 (2018).
- 835 24. Rigort, A. *et al.* Focused ion beam micromachining of eukaryotic cells for cryoelectron tomography.
836 *Proc. Natl. Acad. Sci.* **109**, 4449–4454 (2012).
- 837 25. Villa, E., Schaffer, M., Plitzko, J. M. & Baumeister, W. Opening windows into the cell: focused-ion-
838 beam milling for cryo-electron tomography. *Curr. Opin. Struct. Biol.* **23**, 771–777 (2013).
- 839 26. de Winter, D. A. M. *et al.* In-situ integrity control of frozen-hydrated, vitreous lamellas prepared by the
840 cryo-focused ion beam-scanning electron microscope. *J. Struct. Biol.* **183**, 11–18 (2013).
- 841 27. Zhang, J., Ji, G., Huang, X., Xu, W. & Sun, F. An improved cryo-FIB method for fabrication of frozen
842 hydrated lamella. *J. Struct. Biol.* **194**, 218–223 (2016).
- 843 28. Burdett, I. D. & Murray, R. G. Electron microscope study of septum formation in *Escherichia coli*
844 strains B and B-r during synchronous growth. *J. Bacteriol.* **119**, 1039–1056 (1974).
- 845 29. Berezuk, A. M., Goodyear, M. & Khursigara, C. M. Site-directed Fluorescence Labeling Reveals a
846 Revised N-terminal Membrane Topology and Functional Periplasmic Residues in the *Escherichia*
847 *coli* Cell Division Protein FtsK. *J. Biol. Chem.* **289**, 23287–23301 (2014).
- 848 30. Yang, X. *et al.* A two-track model for the spatiotemporal coordination of bacterial septal cell wall
849 synthesis revealed by single-molecule imaging of FtsW. *Nat. Microbiol.* **6**, 584–593 (2021).
- 850 31. Burman, L. G. & Park, J. T. Molecular model for elongation of the murein sacculus of *Escherichia*
851 *coli*. *Proc. Natl. Acad. Sci. U. S. A.* **81**, 1844–1848 (1984).
- 852 32. Taguchi, A. *et al.* FtsW is a peptidoglycan polymerase that is functional only in complex with its
853 cognate penicillin-binding protein. *Nat. Microbiol.* **4**, 587–594 (2019).
- 854 33. Weiss, D. S. *et al.* Localization of the *Escherichia coli* cell division protein FtsI (PBP3) to the division
855 site and cell pole. *Mol. Microbiol.* **25**, 671–681 (1997).
- 856 34. Du, S. & Lutkenhaus, J. Assembly and Activation of the *Escherichia coli* Divisome. *Mol. Microbiol.*
857 **105**, 177–187 (2017).
- 858 35. Liu, B., Persons, L., Lee, L. & Boer, P. A. J. de. Roles for both FtsA and the FtsBLQ subcomplex in
859 FtsN-stimulated cell constriction in *Escherichia coli*. *Mol. Microbiol.* **95**, 945–970 (2015).
- 860 36. Park, K.-T., Du, S. & Lutkenhaus, J. Essential Role for FtsL in Activation of Septal Peptidoglycan
861 Synthesis. *mBio* **11**, e03012-20.
- 862 37. Tsang, M.-J. & Bernhardt, T. G. A role for the FtsQLB complex in cytokinetic ring activation revealed
863 by an ftsL allele that accelerates division. *Mol. Microbiol.* **95**, 925–944 (2015).
- 864 38. Marmont, L. S. & Bernhardt, T. G. A conserved subcomplex within the bacterial cytokinetic ring
865 activates cell wall synthesis by the FtsW-FtsI synthase. *Proc. Natl. Acad. Sci. U. S. A.* **117**, 23879–
866 23885 (2020).
- 867 39. Gerding, M. A. *et al.* Self-Enhanced Accumulation of FtsN at Division Sites and Roles for Other
868 Proteins with a SPOR Domain (DamX, DedD, and RipA) in *Escherichia coli* Cell Constriction. *J.*
869 *Bacteriol.* **191**, 7383–7401 (2009).
- 870 40. Ursinus, A. *et al.* Murein (peptidoglycan) binding property of the essential cell division protein FtsN
871 from *Escherichia coli*. *J. Bacteriol.* **186**, 6728–6737 (2004).
- 872 41. Yahashiri, A., Jorgenson, M. A. & Weiss, D. S. Bacterial SPOR domains are recruited to septal
873 peptidoglycan by binding to glycan strands that lack stem peptides. *Proc. Natl. Acad. Sci. U. S. A.*
874 **112**, 11347–11352 (2015).
- 875 42. Heidrich, C. *et al.* Involvement of N-acetylmuramyl-L-alanine amidases in cell separation and
876 antibiotic-induced autolysis of *Escherichia coli*. *Mol. Microbiol.* **41**, 167–178 (2001).
- 877 43. Uehara, T., Parzych, K. R., Dinh, T. & Bernhardt, T. G. Daughter cell separation is controlled by
878 cytokinetic ring-activated cell wall hydrolysis. *EMBO J.* **29**, 1412–1422 (2010).

- 879 44. Uehara, T., Dinh, T. & Bernhardt, T. G. LytM-domain factors are required for daughter cell separation
880 and rapid ampicillin-induced lysis in *Escherichia coli*. *J. Bacteriol.* **191**, 5094–5107 (2009).
- 881 45. Ishino, F. *et al.* New mutations *fts-36*, *lts-33*, and *ftsW* clustered in the *mra* region of the *Escherichia*
882 *coli* chromosome induce thermosensitive cell growth and division. *J. Bacteriol.* **171**, 5523–5530
883 (1989).
- 884 46. Ueki, M., Wachi, M., Jung, H. K., Ishino, F. & Matsushashi, M. *Escherichia coli mraR* gene involved in
885 cell growth and division. *J. Bacteriol.* **174**, 7841–7843 (1992).
- 886 47. Kuru, E. *et al.* In Situ Probing of Newly Synthesized Peptidoglycan in Live Bacteria with Fluorescent
887 D-Amino Acids. *Angew. Chem. Int. Ed.* **51**, 12519–12523 (2012).
- 888 48. Hsu, Y.-P., Booher, G., Egan, A., Vollmer, W. & VanNieuwenhze, M. S. d-Amino Acid Derivatives as
889 in Situ Probes for Visualizing Bacterial Peptidoglycan Biosynthesis. *Acc. Chem. Res.* **52**, 2713–
890 2722 (2019).
- 891 49. Bartlett, T. M. *et al.* A Periplasmic Polymer Curves *Vibrio cholerae* and Promotes Pathogenesis. *Cell*
892 **168**, 172–185.e15 (2017).
- 893 50. Liang, H. *et al.* Metabolic labelling of the carbohydrate core in bacterial peptidoglycan and its
894 applications. *Nat. Commun.* **8**, 15015 (2017).
- 895 51. Hale, C. A. & de Boer, P. A. Direct binding of FtsZ to ZipA, an essential component of the septal ring
896 structure that mediates cell division in *E. coli*. *Cell* **88**, 175–185 (1997).
- 897 52. Buss, J. *et al.* In vivo organization of the FtsZ-ring by ZapA and ZapB revealed by quantitative super-
898 resolution microscopy. *Mol. Microbiol.* **89**, 1099–1120 (2013).
- 899 53. Squyres, G. R. *et al.* Single-molecule imaging reveals that Z-ring condensation is essential for cell
900 division in *Bacillus subtilis*. *Nat. Microbiol.* **6**, 553–562 (2021).
- 901 54. Begg, K. J. *et al.* The balance between different peptidoglycan precursors determines whether
902 *Escherichia coli* cells will elongate or divide. *J. Bacteriol.* **172**, 6697–6703 (1990).
- 903 55. Lleo, M. M., Canepari, P. & Satta, G. Bacterial cell shape regulation: testing of additional predictions
904 unique to the two-competing-sites model for peptidoglycan assembly and isolation of conditional
905 rod-shaped mutants from some wild-type cocci. *J. Bacteriol.* **172**, 3758–3771 (1990).
- 906 56. Domínguez-Escobar, J. *et al.* Processive movement of MreB-associated cell wall biosynthetic
907 complexes in bacteria. *Science* **333**, 225–228 (2011).
- 908 57. Garner, E. C. *et al.* Coupled, circumferential motions of the cell wall synthesis machinery and MreB
909 filaments in *B. subtilis*. *Science* **333**, 222–225 (2011).
- 910 58. van Teeffelen, S. *et al.* The bacterial actin MreB rotates, and rotation depends on cell-wall assembly.
911 *Proc. Natl. Acad. Sci. U. S. A.* **108**, 15822–15827 (2011).
- 912 59. Dion, M. F. *et al.* *Bacillus subtilis* cell diameter is determined by the opposing actions of two distinct
913 cell wall synthetic systems. *Nat. Microbiol.* **4**, 1294–1305 (2019).
- 914 60. Hussain, S. *et al.* MreB filaments align along greatest principal membrane curvature to orient cell wall
915 synthesis. *eLife* **7**, e32471 (2018).
- 916 61. Ursell, T. S. *et al.* Rod-like bacterial shape is maintained by feedback between cell curvature and
917 cytoskeletal localization. *Proc. Natl. Acad. Sci. U. S. A.* **111**, E1025–1034 (2014).
- 918 62. Dubochet, J., McDowell, A. W., Menge, B., Schmid, E. N. & Lickfeld, K. G. Electron microscopy of
919 frozen-hydrated bacteria. *J. Bacteriol.* **155**, 381 (1983).
- 920 63. Matias, V. R. F., Al-Amoudi, A., Dubochet, J. & Beveridge, T. J. Cryo-Transmission Electron
921 Microscopy of Frozen-Hydrated Sections of *Escherichia coli* and *Pseudomonas aeruginosa*. *J.*
922 *Bacteriol.* **185**, 6112–6118 (2003).
- 923 64. Zuber, B. *et al.* Direct visualization of the outer membrane of mycobacteria and corynebacteria in
924 their native state. *J. Bacteriol.* **190**, 5672–5680 (2008).

- 925 65. Yao, Q. *et al.* Short FtsZ filaments can drive asymmetric cell envelope constriction at the onset of
926 bacterial cytokinesis. *EMBO J.* **36**, 1577–1589 (2017).
- 927 66. Zhou, X. *et al.* Mechanical crack propagation drives millisecond daughter cell separation in
928 *Staphylococcus aureus*. *Science* **348**, 574–578 (2015).
- 929 67. Truong, T. T., Vettiger, A. & Bernhardt, T. G. Cell division is antagonized by the activity of
930 peptidoglycan endopeptidases that promote cell elongation. *Mol. Microbiol.* **114**, 966–978 (2020).
- 931 68. Paradis-Bleau, C. *et al.* Lipoprotein cofactors located in the outer membrane activate bacterial cell
932 wall polymerases. *Cell* **143**, 1110–1120 (2010).
- 933 69. Typas, A. *et al.* Regulation of peptidoglycan synthesis by outer-membrane proteins. *Cell* **143**, 1097–
934 1109 (2010).
- 935 70. Liu, B., Hale, C. A., Persons, L., Phillips-Mason, P. J. & de Boer, P. A. J. Roles of the DedD Protein
936 in *Escherichia coli* Cell Constriction. *J. Bacteriol.* **201**, e00698-18 (2019).
- 937 71. Yakhnina, A. A., McManus, H. R. & Bernhardt, T. G. The cell wall amidase AmiB is essential for
938 *Pseudomonas aeruginosa* cell division, drug resistance and viability. *Mol. Microbiol.* **97**, 957–973
939 (2015).
- 940 72. Busiek, K. K. & Margolin, W. A role for FtsA in SPOR-independent localization of the essential
941 *Escherichia coli* cell division protein FtsN. *Mol. Microbiol.* **92**, 1212–1226 (2014).
- 942 73. Lyu, Z. *et al.* FtsN activates septal cell wall synthesis by forming a processive complex with the
943 septum-specific peptidoglycan synthase in *E. coli*. 2021.08.23.457437
944 <https://www.biorxiv.org/content/10.1101/2021.08.23.457437v1> (2021)
945 doi:10.1101/2021.08.23.457437.
- 946 74. Coltharp, C., Buss, J., Plumer, T. M. & Xiao, J. Defining the rate-limiting processes of bacterial
947 cytokinesis. *Proc. Natl. Acad. Sci.* **113**, E1044–E1053 (2016).
- 948 75. Rohs, P. D. A. *et al.* A central role for PBP2 in the activation of peptidoglycan polymerization by the
949 bacterial cell elongation machinery. *PLoS Genet.* **14**, e1007726 (2018).
- 950 76. Miller, J. H. *Experiments in molecular genetics*. (Cold Spring Harbor Laboratory, 1972).
- 951 77. Datsenko, K. A. & Wanner, B. L. One-step inactivation of chromosomal genes in *Escherichia coli* K-
952 12 using PCR products. *Proc. Natl. Acad. Sci. U. S. A.* **97**, 6640–6645 (2000).
- 953 78. Dubochet, J. *et al.* Cryo-electron microscopy of vitrified specimens. *Q. Rev. Biophys.* **21**, 129–228
954 (1988).
- 955 79. Wolff, G. *et al.* Mind the gap: Micro-expansion joints drastically decrease the bending of FIB-milled
956 cryo-lamellae. *J. Struct. Biol.* **208**, 107389 (2019).
- 957 80. Wagner, F. R. *et al.* Preparing samples from whole cells using focused-ion-beam milling for cryo-
958 electron tomography. *Nat. Protoc.* **15**, 2041–2070 (2020).
- 959 81. Mastronarde, D. N. SerialEM: A Program for Automated Tilt Series Acquisition on Tecnai
960 Microscopes Using Prediction of Specimen Position. *Microsc. Microanal.* **9**, 1182–1183 (2003).
- 961 82. Hagen, W. J. H., Wan, W. & Briggs, J. A. G. Implementation of a cryo-electron tomography tilt-
962 scheme optimized for high resolution subtomogram averaging. *J. Struct. Biol.* **197**, 191–198 (2017).
- 963 83. Kremer, J. R., Mastronarde, D. N. & McIntosh, J. R. Computer visualization of three-dimensional
964 image data using IMOD. *J. Struct. Biol.* **116**, 71–76 (1996).
- 965 84. Mastronarde, D. N. & Held, S. R. Automated tilt series alignment and tomographic reconstruction in
966 IMOD. *J. Struct. Biol.* **197**, 102–113 (2017).
- 967 85. Xiong, Q., Mophew, M. K., Schwartz, C. L., Hoenger, A. H. & Mastronarde, D. N. CTF Determination
968 and Correction for Low Dose Tomographic Tilt Series. *J. Struct. Biol.* **168**, 378–387 (2009).
- 969 86. Castaño-Díez, D., Kudryashev, M., Arheit, M. & Stahlberg, H. Dynamo: A flexible, user-friendly
970 development tool for subtomogram averaging of cryo-EM data in high-performance computing
971 environments. *J. Struct. Biol.* **178**, 139–151 (2012).

- 972 87. Castaño-Díez, D. The Dynamo package for tomography and subtomogram averaging: components
973 for MATLAB, GPU computing and EC2 Amazon Web Services. *Acta Crystallogr. Sect. Struct. Biol.*
974 **73**, (2017).
- 975 88. Castaño-Díez, D., Kudryashev, M. & Stahlberg, H. Dynamo Catalogue: Geometrical tools and data
976 management for particle picking in subtomogram averaging of cryo-electron tomograms. *J. Struct.*
977 *Biol.* **197**, 135–144 (2017).
- 978 89. Navarro, P. P., Stahlberg, H. & Castaño-Díez, D. Protocols for Subtomogram Averaging of
979 Membrane Proteins in the Dynamo Software Package. *Front. Mol. Biosci.* **5**, (2018).
- 980 90. Koenderink, J. J. & van Doorn, A. J. Surface shape and curvature scales. *Image Vis. Comput.* **10**,
981 557–564 (1992).
- 982 91. Schindelin, J. *et al.* Fiji: an open-source platform for biological-image analysis. *Nat. Methods* **9**, 676–
983 682 (2012).
- 984 92. Ringel, P. D., Hu, D. & Basler, M. The Role of Type VI Secretion System Effectors in Target Cell
985 Lysis and Subsequent Horizontal Gene Transfer. *Cell Rep.* **21**, 3927–3940 (2017).
- 986 93. Mangeol, P., Prevo, B. & Peterman, E. J. G. KymographClear and KymographDirect: two tools for
987 the automated quantitative analysis of molecular and cellular dynamics using kymographs. *Mol.*
988 *Biol. Cell* **27**, 1948–1957 (2016).
- 989 94. Söderström, B., Chan, H., Shilling, P. J., Skoglund, U. & Daley, D. O. Spatial separation of FtsZ and
990 FtsN during cell division. *Mol. Microbiol.* **107**, 387–401 (2018).
- 991 95. Bisson-Filho, A. W. *et al.* Treadmilling by FtsZ filaments drives peptidoglycan synthesis and bacterial
992 cell division. *Science* **355**, 739–743 (2017).
- 993 96. Ursell, T. *et al.* Rapid, precise quantification of bacterial cellular dimensions across a genomic-scale
994 knockout library. *BMC Biol.* **15**, 17 (2017).
- 995 97. Squyres, G. R. *et al.* Single-molecule imaging reveals that Z-ring condensation is essential for cell
996 division in *Bacillus subtilis*. *Nat. Microbiol.* **6**, 553–562 (2021).
- 997 98. Liang, H. *et al.* Metabolic labelling of the carbohydrate core in bacterial peptidoglycan and its
998 applications. *Nat. Commun.* **8**, 15015 (2017).
- 999 99. Yang, X. *et al.* A two-track model for the spatiotemporal coordination of bacterial septal cell wall
000 synthesis revealed by single-molecule imaging of FtsW. *Nat. Microbiol.* 1–10 (2021)
001 doi:10.1038/s41564-020-00853-0.
- 002 100. Fumeaux, C. & Bernhardt, T. G. Identification of MupP as a New Peptidoglycan Recycling Factor
003 and Antibiotic Resistance Determinant in *Pseudomonas aeruginosa*. *mBio* **8**, (2017).
- 004 101. Ball, G. *et al.* SIMcheck: a Toolbox for Successful Super-resolution Structured Illumination
005 Microscopy. *Sci. Rep.* **5**, 15915 (2015).
- 006 102. Tinevez, J.-Y. *et al.* TrackMate: An open and extensible platform for single-particle tracking.
007 *Methods San Diego Calif* **115**, 80–90 (2017).
- 008 103. Tarantino, N. *et al.* TNF and IL-1 exhibit distinct ubiquitin requirements for inducing NEMO–IKK
009 supramolecular structures. *J. Cell Biol.* **204**, 231–245 (2014).
010

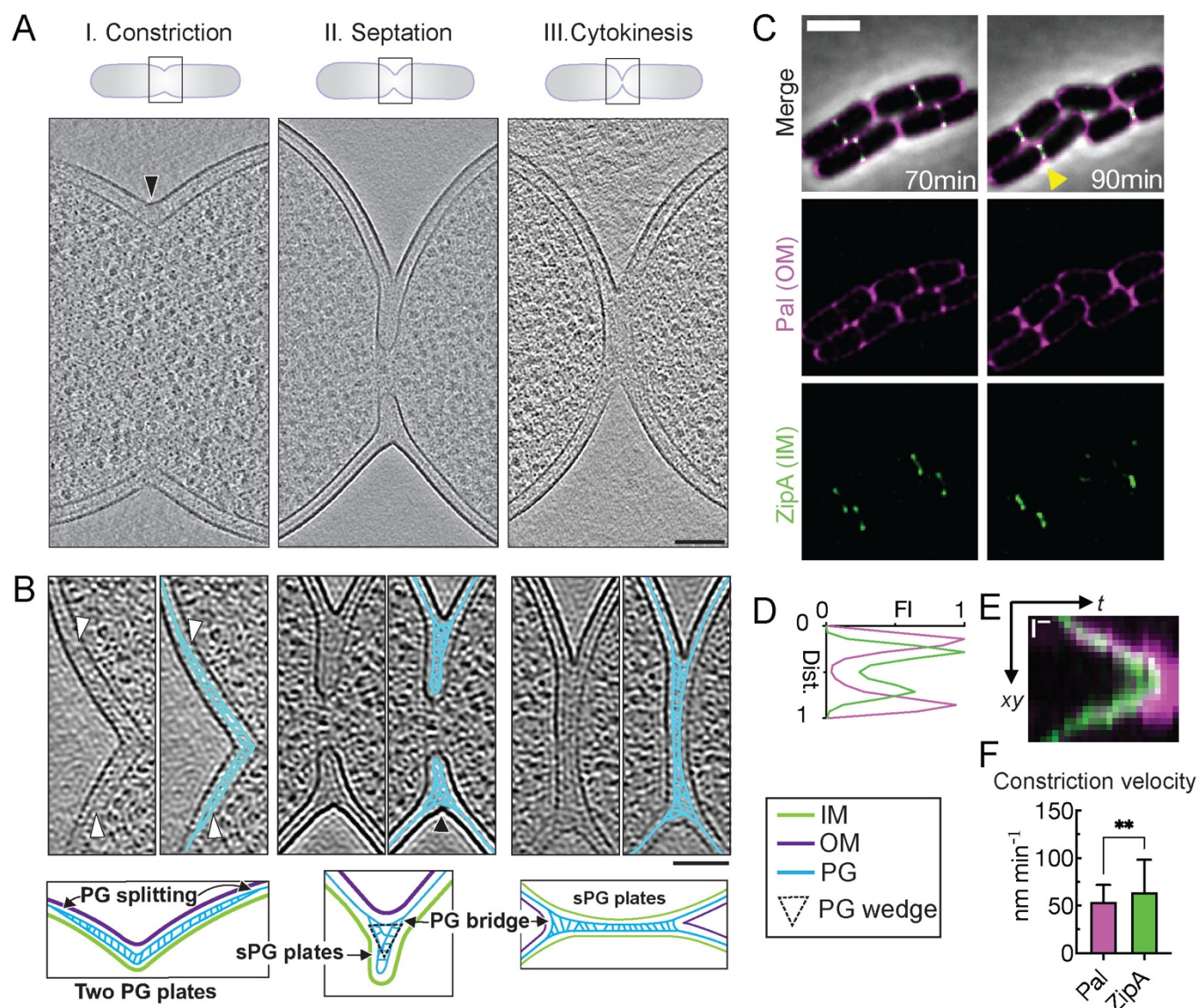


Figure 1: *In situ* cell envelope architecture and dynamics during *E. coli* cell division. (A) Overview of different stages of cell division. Summed, projected central slices of cryo-electron tomograms visualizing different stages in division of wild-type *E. coli* are shown. Black arrowhead indicates division site side displayed in B. (B) NAD-filtered cryo-electron tomograms visualizing the cell wall. Left panels show a 3D slice, right panels show the corresponding slice with segmented PG signal in cyan (see Methods). White arrowheads indicate where the PG layer appears to thicken from one to two layers, and black arrowhead indicates division site side shown in the schematic overview for the septation stage of the visualized cell envelope architecture. (C) Time-lapse series of wild-type *E. coli* expressing Pal-mCherry and ZipA-sfGFP as OM and IM markers, respectively, imaged at 30°C on M9 supplemented with 0.2% casamino acids and D-glucose. Fluorescence signals were deconvolved (see Methods). Yellow triangles mark division sites used for line scans of fluorescence intensity profiles (D) and kymograph analysis of cytokinesis (E). (F) Constriction velocity of IM and OM were derived from the slopes of the fluorescence signals in kymographs (see Methods). All data are expressed as mean + one SD. Two-sided unpaired t-test; ** $p < 0.01$; $N = 150$ division kymographs. Scale bar: (A) and (B) = 100 nm, (C) = 2 μm , and (E) = 200 nm (vertical); 5 min (horizontal).

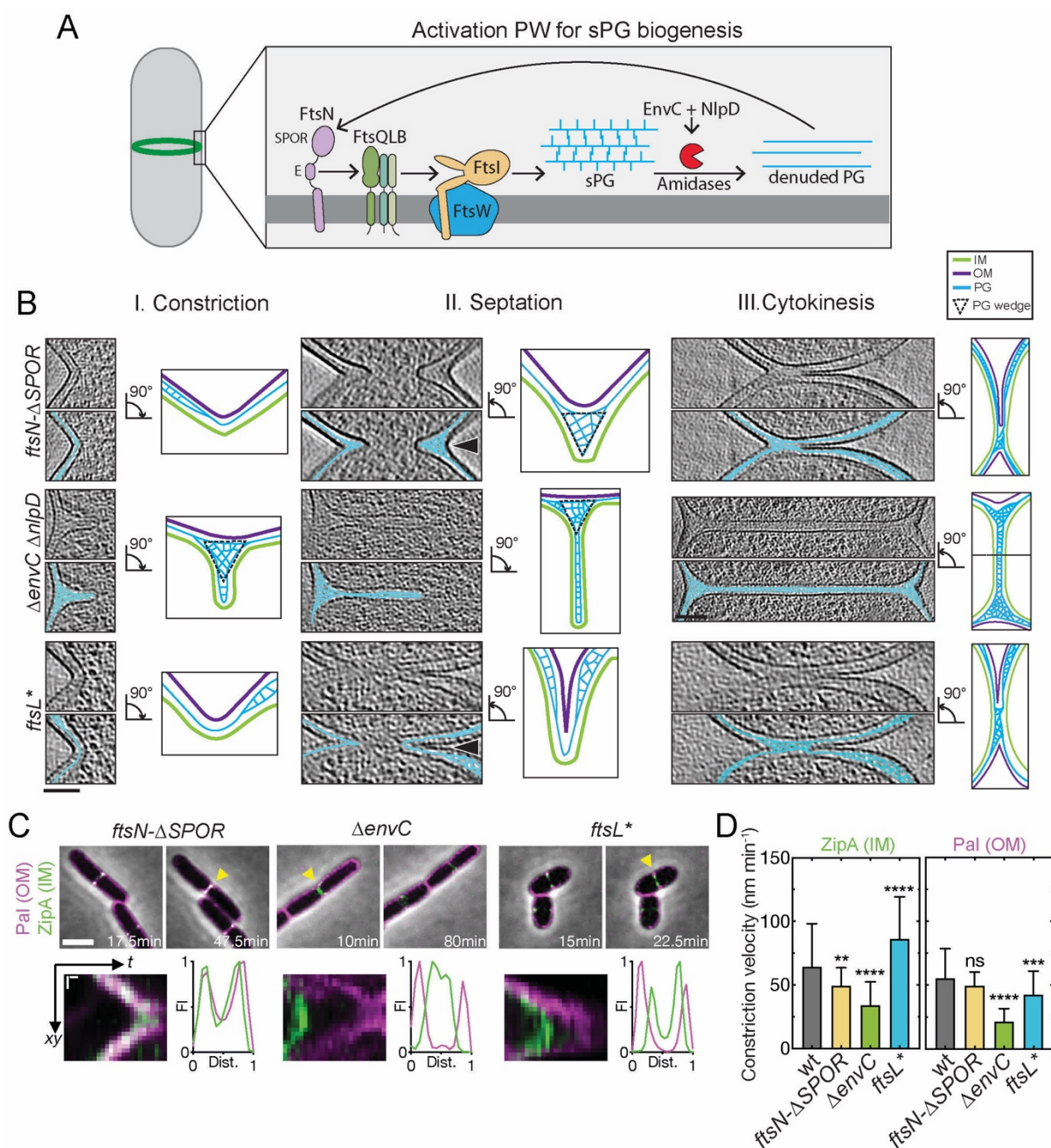


Figure 2: Divisome mutants display altered division site ultrastructure and constriction kinetics.

(A) Schematic overview of the septal PG loop pathway for the activation of sPG synthesis (see text for details). (B) NAD-filtered cryo-electron tomograms of division sites in the indicated division mutants of *E. coli*. Top panels show a 3D slice and bottom panels show the corresponding slice with segmented PG signal in cyan (see Methods). Right panels show summary diagrams of the cell envelope architecture visualized by cryo-ET. Black arrowheads indicate division site side represented in the schemes. (C) Time-lapse series of indicated *E. coli* division mutants expressing Pal-mCherry and ZipA-sfGFP as OM and IM markers, respectively, imaged as in Figure 1. Yellow triangles mark division sites used for kymograph analysis and line scans of fluorescence intensity profiles of cytokinesis. (D) Constriction velocity of the IM and OM were determined as in Figure 1. All data are expressed as mean + one SD. Data from wild-type is replotted from Fig. 1F for comparison. Brown-Forsythe and Welch ANOVA tests, differences in significances are tested relative to wild-type; ** $p < 0.01$, *** = $p < 0.001$, **** $p < 0.0001$; N = 150 division kymographs for each strain. Scale bar: (B) = 100 nm and (C) top row = 2 μ m and bottom row kymographs = 200 nm (vertical); 5 min (horizontal).

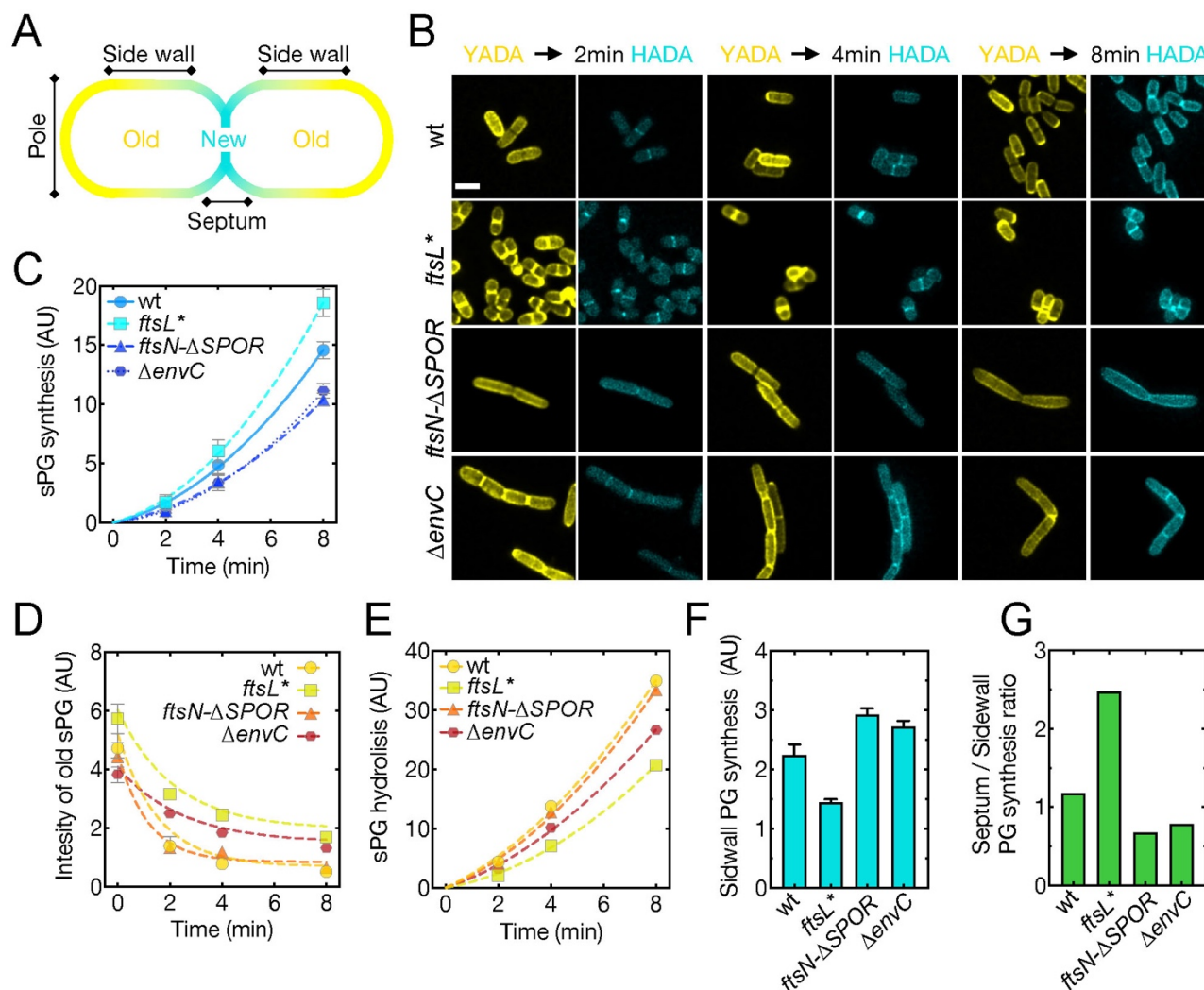


Figure 3: FDAA assay for cell wall synthesis and hydrolysis rates during division and elongation.

(A) Schematic representation of labeling patterns observed for the pulse-chase experiment. New cell wall material is labeled with HADA (blue), while old material is stained with YADA (yellow). (B) Representative images of indicated strains after 2, 4 and 8 min pulses with HADA. Integrated fluorescence intensity was measured and normalized at the division site area for new (C) and old (D) PG. Deriving the integral from these intensity measurements yields the rate of sPG synthesis. Data was fit to a quadratic exponential equation (R -squared > 0.9). (E) Septal PG hydrolysis rates were derived from calculating the reduction in YADA fluorescence intensity over time, as compared to cells fixed prior to chase (time point 0 min, D). (F) Sidewall incorporation of new cell wall material (HADA fluorescence intensity) was measured after 8 min, due low signal intensities in earlier timepoints. (G) Ratio between sPG and sidewall synthesis was calculated by dividing the mean HADA fluorescence intensity for each after the 8 min pulse. All data are represented as mean fluorescence intensity. Error bars represent 95 % confidence intervals. All values are arbitrary fluorescence intensity units and were divided by 1000 for plotting purposes. Scale bar in (A) = 2 μ m.

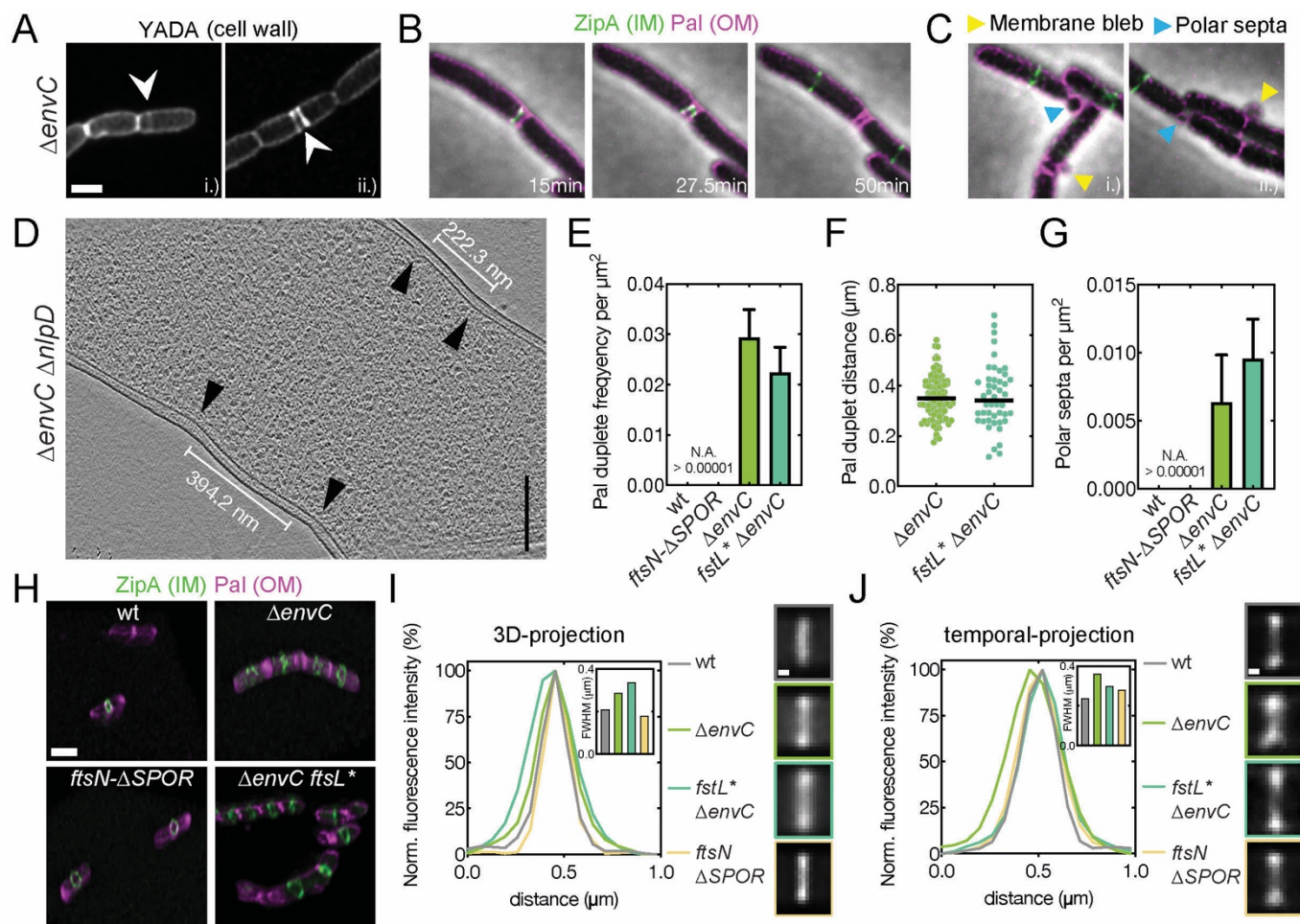


Figure 4: sPG hydrolysis is required for normal Z-ring placement and condensation. (A) Distribution of cell wall material in $\Delta envC$ cells was assessed by FDAA staining. Images are sum-projections of a 1 μm spanning z-stack and were deconvolved. White arrowheads indicated double septa. (B) Time-lapse series of a $\Delta envC$ mutant expressing Pal-mCherry and ZipA-sfGFP as OM and IM markers, respectively, imaged as in Figure 1. An example of double septum formation is shown. (C) Examples for membrane blebbing (yellow arrowheads) and polar septa (blue arrowheads) formation are highlighted. (D) Formation of double constrictions observed in cryo-electron tomograms of $\Delta envC \Delta nlpD$ cells. (E) Frequency of double septum formation was quantified from counting the number of Pal-mCherry doublets and normalizing for cell area. No Pal doublets were found > 10,000 cells for wild-type or *ftsN*- $\Delta SPOR$ cells. Data is represented as mean + SD. (F) Distance between Pal duplets was measured manually using the line tool in Fiji. (G) Frequency of polar septa was measured for the indicated strains and normalized per cell area. No polar septa were observed in > 10,000 wild-type or *ftsN*- $\Delta SPOR$ cells. (H) Three-dimensional maximum intensity renderings showing Z-ring condensation based on ZipA-sfGFP localization. Scale bar = 2 μm . The degree of Z-ring condensation was quantified from averaged fluorescence intensity projections from summed 3D volumes (I) or from 5 time points (corresponding to 10 min) of a time-lapse series (J). Width of the fluorescence signal distribution across the horizontal axis was used to determine degree of condensation. FWHM is shown as an insert. Averaged Z-rings are shown and color-coded according to graphs. Scale bars: (A)-(C) = 2 μm , (D) = 200 nm, (H) = 2 μm , (I)-(J) = 200 nm.

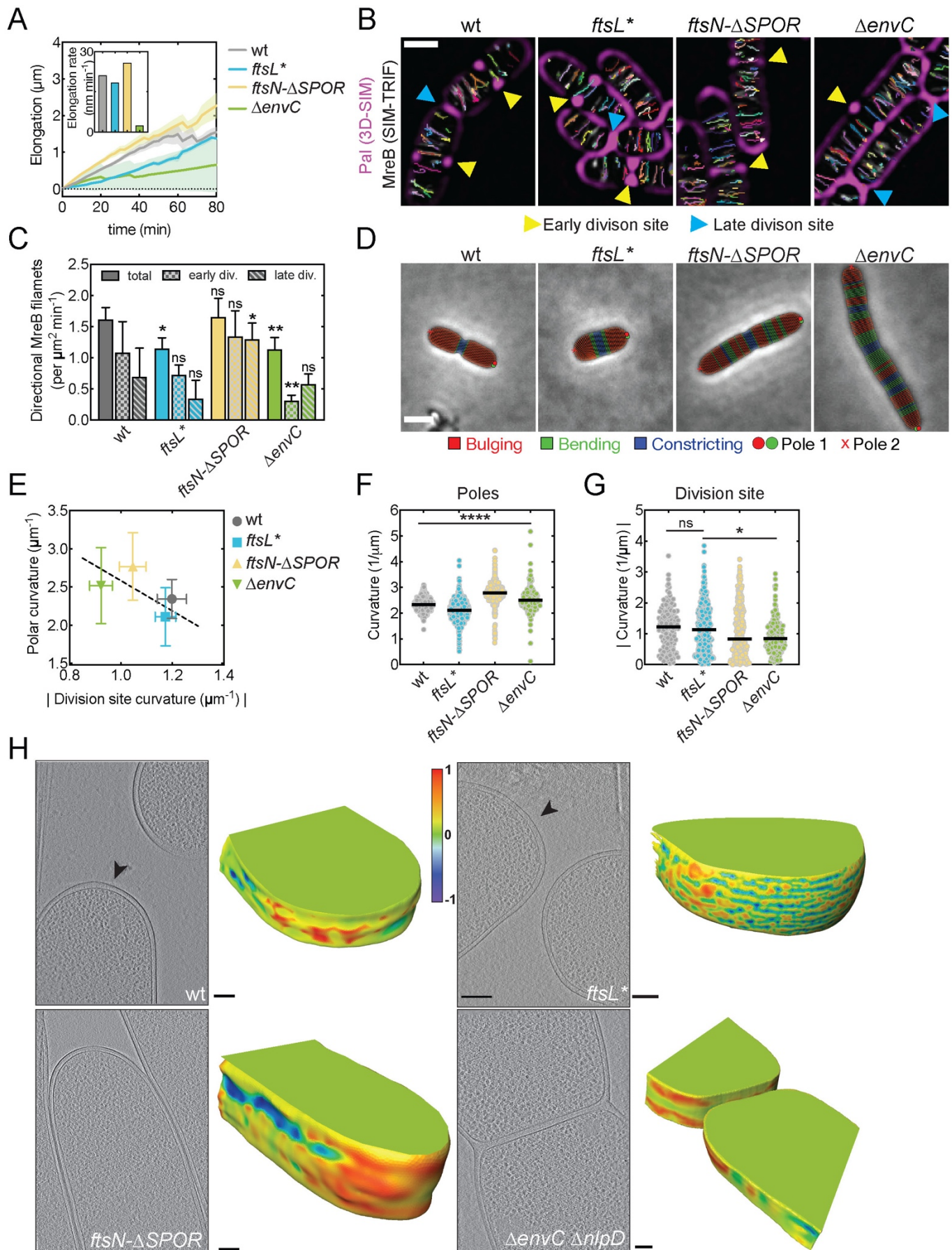


Figure 5: Competition between the divisome and elongation machinery defines polar cell shape. (A) Single-cell elongation was measured for indicated mutants grown at 30°C on M9 supplemented with 0.2% casamino acids and D-glucose for 80 min. Elongation rate (insert) was determined from the slope of a best fit linear regression model. (B) MreB dynamics were followed using an mNeonGreen sandwich fusion (MreB^{sw-mNG}) in the indicated strains for 3 min at 3 second acquisition frame rate using SIM-TIRF microscopy. Time-lapse series were sum projected and overlaid with single particle tracking results from TrackMate and 3D-SIM Pal-mCherry reference images. Pal-mCherry signal serves to identify constricted cells. Early division site (yellow arrowheads) displayed Pal foci which were resolvable as two distinct foci, whereas late division sites (blue arrowheads) displayed a continuous Pal signal across the cell body, indicative of complete or near complete cytokinesis. (C) Directionally moving MreB tracks were filtered by MSD analysis (see Methods) and plotted as mean + SD and normalized by cell area. One-way ANOVA test, differences in significances are tested relative to wild-type for each corresponding stage; * p < 0.05, ** p < 0.01, ns = non-significant. (D) Representative phase contrast micrographs showing segmented cells in *Morphometrics* for the indicated division mutants. Color-coded legend indicates cell regions with positive curvature on both sides (red, bulging), negative curvature on both sides (blue, constricting) and positive curvature on one side while negative curvature on the other side (green, bending). Red dots indicate poles. Scale bar = 2 µm. (E-G) Polar curvature was measured by the two highest points of positive cell outline curvature, while constriction curvature was assessed by measuring the opposing contour-matched lowest curvature values at the division site using *Morphometrics* (see Methods). Polar and division site curvatures are negatively correlated. Ordinary One-way ANOVA; * p < 0.05, **** p < 0.0001, ns = non-significant. (H) Summed, projected central 3D slices through cryo-electron tomograms visualizing cell poles. Black arrowheads indicate 3D rendered pole. The corresponding 3D-volume renderings show the type of curvature present on the pole surface determined by shape index (see Methods). Summed projection images are scaled. Scale bars: (B) = 1 µm, (D) = 2 µm (H) summed projection images = 200 nm and 3D renderings = 100 nm.

.011

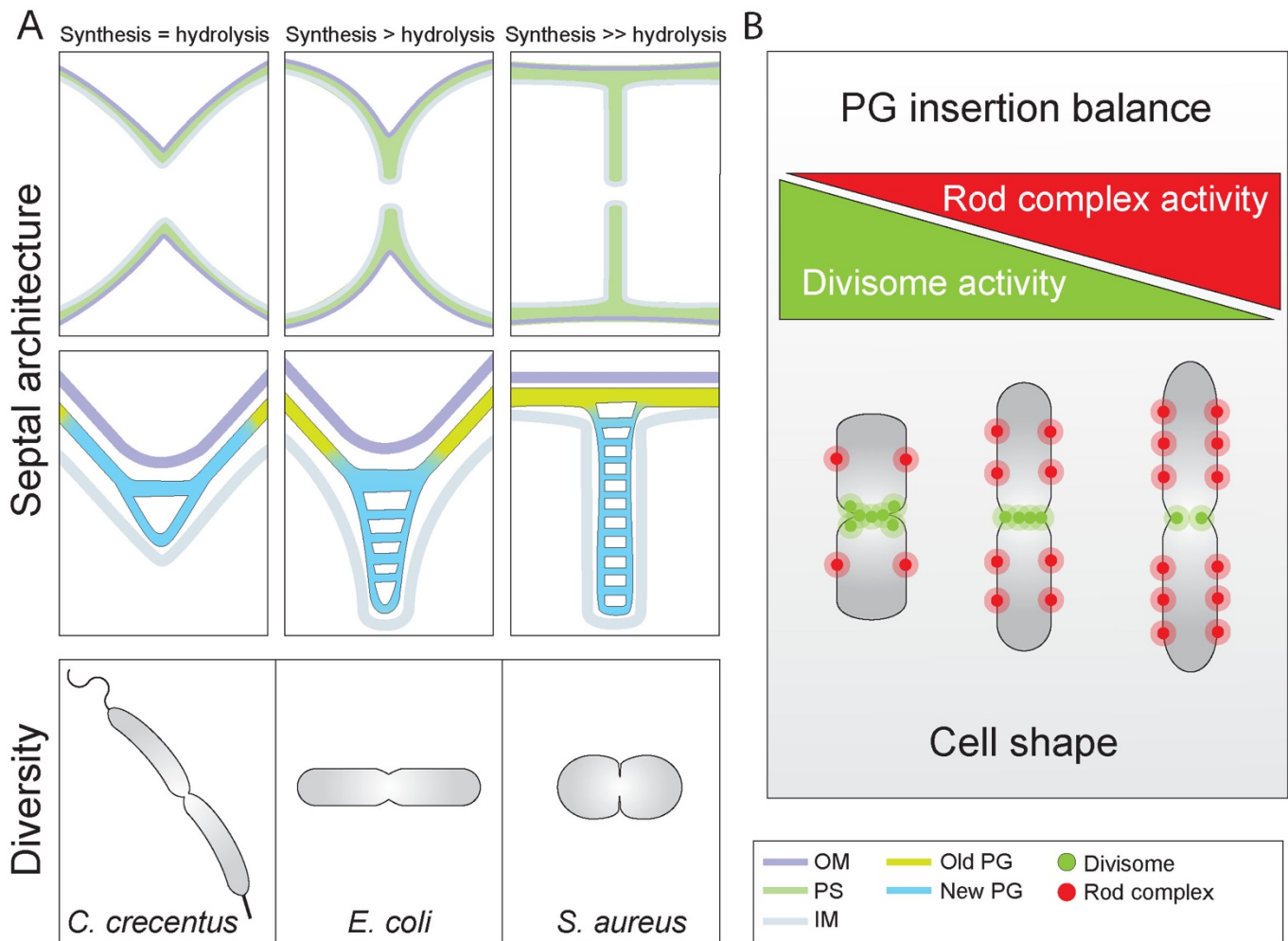


Figure 6: Septal PG architecture and divisome activity modulate bacterial morphogenesis. (A) A wide range of different sPG architectures can result from the same division machinery through altering rates of cell wall synthesis and hydrolysis. Constrictive mode of cell division where OM and IM invaginate at similar velocities, a phenotype commonly associated with *C. crescentus*, is the result of lower sPG synthesis rates. Here, the septal cell wall displays a V-shaped wedge where no sPG plates are present. In contrast, inhibition of sPG hydrolysis causes a temporal separation of IM and OM constriction leading to septation. These septa are reminiscent to those of Gram-positive bacteria such as *S. aureus*, displaying two distinctive plates of sPG linked together by a PG bridge. Wild-type *E. coli* displays a mixed constriction-septation phenotype resulting in a partial septum at later stages of the division process. (B) The activities of the two major synthetic cell wall machineries, the Rod complex and the divisome, are anticorrelated, likely due to competition for limited substrate (lipid II). Balance of their relative activities determines the shape of the cell division site and the resulting poles they form. Cells with higher Rod complex activity are thinner and form pointier poles, while cells with elevated divisome activity are shorter and wider with blunt poles.